

Copyright

by

Paul Vincent Van Noordt

2009

**A New Approach to Modeling Drop-Pair Collisions:
Predicting the Outcome through a Fluidic-Mechanical
System Analogy**

by

Paul Vincent Van Noordt, B.S.

Thesis

Presented to the Faculty of the Graduate School of
The University of Texas at Austin
in Partial Fulfillment
of the Requirements
for the Degree of

Master of Science in Engineering

The University of Texas at Austin

August 2009

**A New Approach to Modeling Drop-Pair Collisions:
Predicting the Outcome through a Fluidic-Mechanical
System Analogy**

**Approved by
Supervising Committee:**

Supervisor: _____

Carlos H. Hidrovo

Alexandre K. da Silva

Acknowledgements

The author would like to thank his advisor, Dr. Carlos Hidrovo, for his guidance throughout this project as well as his many contributions to the work. He would also like to thank his friends and family for their support as well as his partner and best friend, Courtney, for her unwavering patience. Finally, the author would like to thank his close friend James Healy (Penn State University) for his invaluable assistance and mentoring not only throughout this project but also throughout the author's academic career.

August 14, 2009

Abstract

A New Approach to Modeling Drop-Pair Collisions: Predicting the Outcome through a Fluidic-Mechanical System Analogy

Paul Vincent Van Noordt, M.S.E.

The University of Texas at Austin, 2009

Supervisor: Carlos H. Hidrovo

A theoretical study of the approach and collision of liquid-drop pairs is performed with results obtained numerically. The collision process is modeled by a squeeze-flow problem involving both planar and non-planar geometry, with attention given to the deformation of the interacting interfaces. Based on the nature of the collision process, an analogy is made between the fluidic systems of colliding liquid bodies and a mechanical mass-spring-damper system. Examination of the analogous mechanical system yields the derivation of an effective damping ratio, ζ^* , which is used to predict the outcome of the drop-drop collisions. Predictions made by utilizing the effective damping ratio are then compared to experimental results presented in literature.

Table of Contents

Chapter 1: Introduction	1
1.1 Motivation	1
1.2 Review of Literature	2
Chapter 2: Theoretical Models	19
2.1 Planar Body Approaching Non-Deformable Surface.....	19
2.2 Planar Body Approaching Deformable Surface.....	26
2.3 Symmetric Approach of Two Deformable Cylindrical Bodies.....	32
Chapter 3: Analogy to Mass-Spring-Damper System	36
3.1 Viscoelasticity and the Maxwell Model.....	36
3.2 Transfer Function Analysis.....	40
3.3 State-Space Approach and Derivation of System Parameters	43
Chapter 4: Numerical Methodology	53
4.1 Numerical Methods and Parameters	53
4.2 Uncertainty Analysis.....	55
Chapter 5: Results and Discussion	57
5.1 Case A: Planar Body Approaching Non-Deformable Surface.....	57
5.2 Case B: Planar Body Approaching Deformable Surface.....	63
5.3 Case C: Symmetric Approach of Two Deformable Cylindrical Bodies.....	76
5.4 Comparison Between Fluidic Models and Analogous Mass-Spring-Damper System	84
5.5 Comparison With Experimental Results	93
Chapter 6: Conclusions	95
Appendices	97
Appendix A: Derivation of Governing Equations for a Disk-Shaped and Cylindrical Body Approaching a Non-Deformable Surface	97
Appendix B: Transfer Function Analysis of Mass-Spring-Damper System.....	102
Appendix C: Matlab® Code	104
References	116
Vita	120

Chapter 1

Introduction

1.1 MOTIVATION

Microfluidics refers to the study of manipulating fluids within networks of very small channels, typically with dimensions of $\sim 5\text{--}500\ \mu\text{m}$. Over the past several decades, the study of microfluidics has gained momentum as it has proven to be of great value in many engineering and scientific applications. Because of the small scales involved, microfluidics requires only small sample sizes, which can result in shorter reaction and analysis times, relatively cheap costs, and little waste. These characteristics of microfluidics make it especially useful in biology, chemistry, and medicine (Weibel & Whitesides, 2006). Other industrial applications of microfluidics include combustion spray systems, ink-jet printing, micro-electromechanical systems (MEMS), as well as microscale total-analysis systems (Micro-TAS) and lab-on-a-chip (LOC) devices.

The purpose of the present study is to investigate the process of two drops colliding head-on in order to gain a better understanding of the mechanisms that govern the outcome of the collision. The relationship between kinetic and surface energy of the colliding drops is considered, as are the properties of the intervening gaseous medium, as factors that govern the outcome. It is widely accepted

that one of four primary outcomes are possible after two drops collide, namely bounce, coalescence, disruption, or fragmentation (Orme, 1997). Consideration of the factors that are believed to govern the collision process allow the development of a criteria that can be used to predict the outcome of the collision under a given set of initial and boundary conditions.

1.2 REVIEW OF LITERATURE

Interest in the collision process of liquid drops dates back as far as 1896 when Lord Rayleigh wrote about the collision of liquid droplets and the influence of electricity on the collision outcome (Rayleigh, 1896). Interest in drop collisions peaked in the early 1960's as investigators became more interested in understanding raindrop formation and the behavior of raindrop interactions during free fall. Many of the early experiments aimed at determining conditions under which water drops falling at terminal velocity would coalesce to form larger drops, as in the formation of precipitation.

Many of the early experimenters focused on the Weber number, $We = \rho V^2 D / \sigma$ (where ρ is the drop density, V is the drop approach velocity, D is the drop diameter, and σ is the drop surface tension), as a characteristic parameter that can be used to predict the outcome of drop-drop

collisions. R.M. Schotland investigated the collision of drops of radii ranging from 100-400 μm onto a hemispherical surface and concluded that the drops tended to coalesce for $We > 3$ (Schotland, 1960). Shortly thereafter, R. Gunn found that pairs of drops with radii, $r = 1 \text{ mm}$ bounced for relative approach velocities of $V < 0.4 \text{ m/s}$, which corresponds to $We < 4$ (Gunn, 1965).

In 1972, P.R. Brazier-Smith, et al. published their work that investigated the interactions of falling water drops of varying radii. The drop radii ranged from 150-750 μm and the relative approach velocities ranged from 0.3-3 m/s. The study revealed four possible outcomes of the drop collisions: bouncing, permanent coalescence, coalescence followed by separation, and coalescence followed by separation and fragmentation, which resulted in the formation of satellite droplets. Based on simple energy concepts, the authors derived an expression for coalescence efficiency,

$$\epsilon = 2.40 \left(\frac{\sigma}{U^2 r \rho} \right) f(R / r) \quad (1)$$

where $f(R/r)$ is a function of the droplet size ratio. Furthermore, they found that an accurate threshold for describing bouncing during the collision of equal-sized

drops is $rU^2\rho/\sigma \sim 2.12$. This states that the collision of two equally sized drops of the same liquid is likely to result in bouncing if the corresponding Weber number (based on drop radius, r) is less than 2.12, or $We < 2.12$. In addition, the effect of drop charge on the collision process was also investigated. (Brazier-Smith, Jennings, & Latham, 1972)

Later, in 1978, S.G. Bradley and C.D. Stow published *Collisions Between Liquid Drops*, in which they reported the results of a series of experiments that investigated the collision between free-falling drops of different sizes. The drops were allowed to reach their terminal velocities, and the trajectory, size, and electric charge of each drop was carefully controlled. The experimental setup utilized synchronized flash photography to obtain images of the collision process. (Bradley & Stow, 1978)

Bradley and Stow attempted to describe the physics of the collision process in terms of an impact parameter, which they denoted as X (the impact parameter is a term that is related to the orientation of the drops during flight), and three different energy parameters: the electrostatic energy, rotational energy, and total energy of the drop system before impact. Depending on the impact parameter, four types of rotational behavior after collision were

observed. For nearly head-on collisions, however, very little rotation was observed in the resulting drop.

Bradley and Stow also performed an analytical study of the film drainage process as a supplement to their experiments. Lord Rayleigh was the first to propose the theory that a thin film of the gaseous medium between colliding drops is responsible for inhibiting coalescence. Since then, Lord Raleigh's theory has become widely accepted among investigators. Bradley and Stow simplified the problem by modeling the collision of disks rather than spherical drops and utilizing the lubrication approximation. Their analysis accounted for interfacial motion as well as surface deformation. Using simple theoretical concepts to model the flattening of the drops, combined with experimental results, the authors formulated a requirement for coalescence:

$$R \leq \frac{1}{4} (3We + 1) \quad (2)$$

where R is the drop radius [mm] and We is the corresponding drop Weber number. One shortcoming of this particular investigation is that the parameter values were limited in order to focus on reproducing atmospheric conditions.

Stergios G. Yiantsios and Robert H. Davis have also studied the approach and collision of two viscous drops

rather extensively. They first analyzed the approach of a viscous drop towards a deformable interface under the constraint of small Bond number, $Bo = \Delta\rho g a^2 / \sigma$, where a is the radius of the drop. The limitation of small Bond number ensured that the deformation of the drop and interface that results from the lubrication force (for an analysis of the lubrication force, see Davis, Schonberg, & Rallison, 1989) remains negligible until the gap between the surfaces is very small. By applying lubrication theory in the thin film between the surfaces and utilizing a boundary integral method to resolve the fluid-phase movement on each side of the film, Yiantsios and Davis showed that a dimple would always form on the surface under sufficiently long approach times. The dimpling allows for the possibility of coalescence via the attraction of the surfaces due to van der Waals forces. (Yiantsios & Davis, 1990)

Yiantsios and Davis later extended their work to include the approach of two viscous drops of different radii under buoyancy-driven axisymmetric motion (Yiantsios & Davis, Close Approach and Deformation of Two Viscous Drops due to Gravity and van der Waals Forces, 1991). Again, they limited the analysis to small capillary number, $Ca = \mu V / \sigma$, and used similar techniques as in their previous work for resolving the flow field within the intervening

film between the drops. They also accounted for the internal circulation of the drops that results from large tangential stresses along the drop surfaces. Numerical calculations were used to track the evolution of the drop shape as well as predict the "rupture time" of the intervening film. The key limitation of both previously discussed analyses performed by Yiantsios and Davis is that the results are valid only within the creeping flow regime, which requires that the Reynolds number of the drops, $Re = \rho V D / \mu$, be much less than 1. This limits the analysis to very slow approach velocities, as found in buoyancy-driven flows. Despite their limitations, Yiantsios and Davis' studies have provided motivation and reference for many other investigators, such as S.A.K. Jeelani and S. Hartland, who followed Yiantsios and Davis' methodology to study the effect of surface mobility on the collision of drop pairs (Jeelani & Hartland, 1998).

Many contemporaries of Yiantsios and Davis were also looking into the collision of liquid drops. For example, N. Ashgriz and J.Y. Poo published their work in 1990, which studied the collisions of water drops with size ratios of 1, 0.75, and 0.5, and with We ranging from 1–100. Ashgriz and Poo concluded that the parameters that most influence the outcome of the collision are the Weber number, the drop-size ratio, and the impact parameter. For equally

sized drops, they found that the collision results in either reflexive separation or stretching separation. Bouncing was not observed under any circumstances. However, for nearly head-on collisions of equal-sized drops, the smallest Weber number imposed was 5, which prohibited the possibility of observing bouncing at lower We values. (Ashgriz & Poo, 1990)

J. Qian and C.K. Law performed what is arguably the most comprehensive and most cited study of drop collisions to date (Qian & Law, 1997). They investigated the dynamics of binary drop collisions by making use of series of time-resolved photographs that captured the collision process. The experiments consisted of both water and hydrocarbon drops colliding within various gases under varying pressures, enabling a wide range of collision conditions to be studied. They found that five regimes of collision outcomes exist: coalescence after minor deformation, bouncing, coalescence after significant deformation, and coalescence followed by separation for both head-on and off-center collisions. Qian and Law created collision maps in terms of the Weber number and impact parameter that show the boundaries between the five different regimes. A representative collision map as created by Qian and Law is shown in Figure 1.

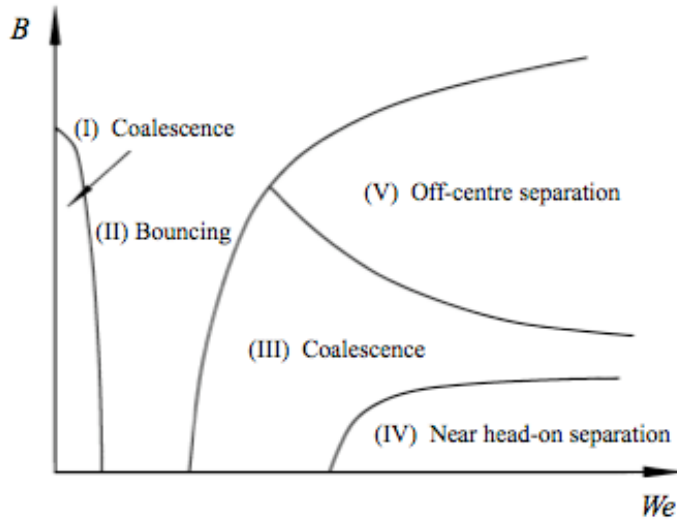


Figure 1: Representative collision map as created by Qian and Law (Qian & Law, 1997).

Although the map in Figure 1 shows a bouncing regime, Qian and Law did not observe bouncing for water droplets under any circumstances. They suggest this is because of the relatively high surface tension and low viscosity of water compared to hydrocarbon, which together act to prohibit the expelling of the gaseous film that acts as a barrier to coalescence. However, they note that bouncing may very well occur for low- We head-on collisions of water drops in a high-pressure gas field, although this particular setup was not investigated.

In addition to capturing photographs of the collision process of liquid drops, Qian and Law also derived a criterion that governs the transition between bouncing and

coalescence. Using simple energy arguments, they found that the critical We beyond which coalescence occurs is dependent on the Ohnesorge number, $Oh = 16\mu/(\rho R\sigma)^{1/2}$; that is

$$We_{crit} = \beta Z + \gamma \quad (3)$$

where Z is the Ohnesorge number, β is a geometry parameter that is independent of the liquid properties, and γ is a term that is related to the surface energy associated with the deformation, and hence the increase in surface area, of the colliding drops.

Melissa Orme published a thorough review of experiments regarding drop collisions in 1997. She compared and contrasted a number of significant experiments to date and found that although many investigators attempted to define the drop-drop collision process in terms of We and an impact parameter, there have been qualitative disagreements concerning the critical We that defines the boundary between the various collision outcome regimes. Orme suggested that one possible reason for discrepancies amongst investigators who worked with similar fluids is that perhaps the presence of surfactants on the drop surfaces affects the collision outcome, a possibility that has been overlooked in many of the experiments she had

reviewed. Orme also noted the significant differences between the behavior of water drops and fuel drops. This finding supports the notion that the behavior of liquid drops depends strongly on the drop surface tension and viscosity, as well as the ambient gas properties, including density, viscosity, and pressure. As a result, the value of the critical We that defines the threshold between the various regimes of the collision will vary with the drop fluid as well as the ambient fluid. (Orme, 1997)

Following Qian and Law, many investigators continued to study the collision of drops of various liquids under a wide range of conditions. For example, J.P. Estrade, et al. studied ethanol drops colliding in air at atmospheric conditions (Estrade, Carentz, Lavergne, & Biscos, 1999). They focused their study on drops of diameter ranging from 80–300 μm with approach velocities of 3–12 m/s. Similar to previous investigators, Estrade, et al. used photographic images of the collision process to determine critical We values separating the various collision regimes.

Additionally, Estrade, et al. also performed an energy analysis to determine a new correlation that predicts bouncing in terms of We . They argued that in order for bouncing to occur, the kinetic energy associated with the deformation of the drops can not exceed the energy that is required to produce a "limit deformation" (Figure 2).

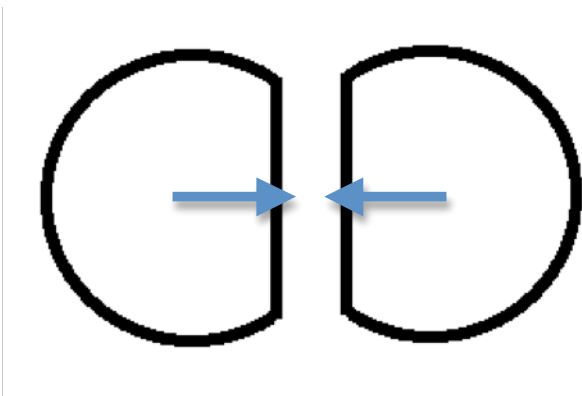


Figure 2: Sketch of drop deformation during bouncing, resulting in a "limit deformation" (Estrade, et al. 1999).

This analysis resulted in a correlation that fit their experimental data very well. The correlation predicted that the critical Weber number, We_{crit} , that separates the bouncing and coalescence regimes is about 2.8, whereas the experimental results indicate that $We_{crit} \sim 4.57$. Although the correlation fit their data well, it disagreed greatly with previous predictions made by Brazier-Smith, et al.

(Brazier-Smith, Jennings, & Latham, 1972). One limitation of this particular experiment is that the experimental setup only permitted bouncing to be observed for nearly head-on collisions with impact parameters of 0.3 or greater (head-on collisions correspond to an impact parameter of 0).

In recent years, investigators began to focus more on creating numerical models to predict the outcome of drop-drop collisions, using the abundance of existing experimental results as a basis of comparison. Scott L. Post and John Abraham (Post & Abraham, 2002) created a composite model that incorporated many of the previous correlations from past studies, such as those of Brazier-Smith's study (Equation (1)). The motivation behind creating a composite model is that, as Qian and Law showed (Qian & Law, 1997), hydrocarbon drops tend to behave very differently than water drops under the same conditions. Therefore, in order to gain a better understanding of drop-drop collisions in diesel sprays, for instance, modifications to the existing correlations that were primarily based on water drops were needed. A comparison of Post and Abraham's analytical composite model to various experimental models is shown in Figure 3.

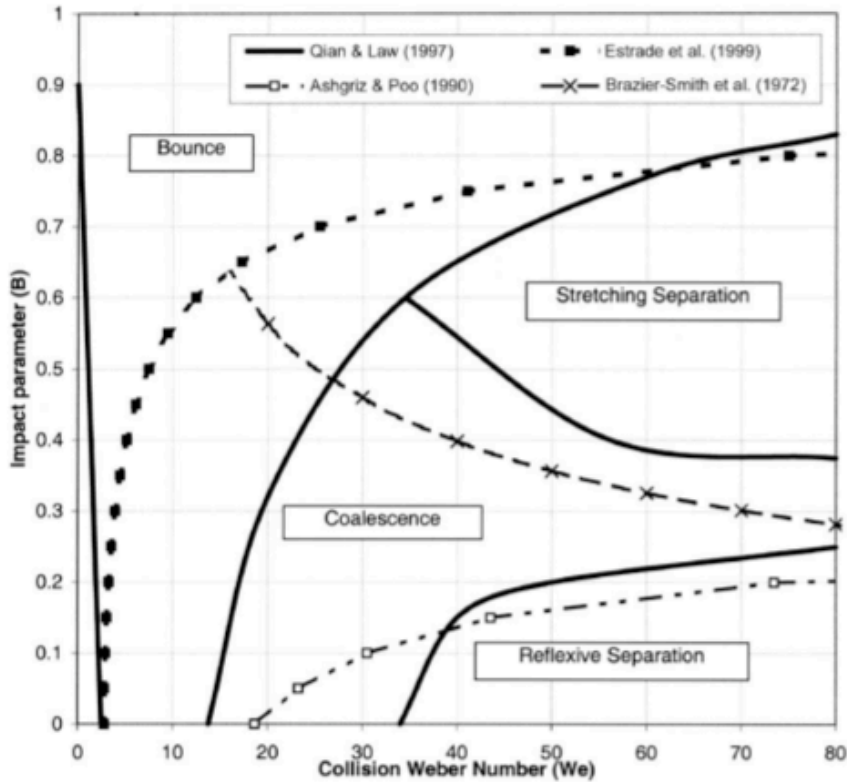


Figure 3: Comparison of analytical and experimental collision maps for equal-sized drops at $P_{\text{atm}} = 1$ bar (Post & Abraham, 2002).

Post and Abraham found that their composite model, which accounted for reflexive separation, rotational separation, as well as bounce, predicted a much lower coalescence rate than did Brazier-Smith's earlier model. As the authors themselves noted, many of the limitations of this study were a result of numerical inadequacies.

Gloria Bach, et al. also studied the collision between small aerosol droplets with an emphasis on determining the

conditions under which the droplets would bounce or coalesce. Bach, et al. experimented with 20 and 40 μm radius water droplets of small We , approximately $O(1)$, as they approached water sublayers under various pressures and viscosities. Using asymptotic theory, which is only valid for small We conditions, they found that the critical Weber number that separates the bouncing and coalescence regimes is strongly dependent on the pressure and viscosity of the ambient gas through which the colliding drops travel. Their findings imply that the collision outcome is much more dependent on the Ohnesorge number, Oh , as well as the Knudsen number, $Kn = \lambda/a$ (where λ is the mean free path of the gaseous medium and a is the drop radius), rather than simply the Weber number of the colliding drops. (Bach, Koch, & Gopinath, 2004)

Yosang Yoon, et al. also studied the coalescence process of two equal-sized drops in an axisymmetric flow by utilizing an integral-boundary method. Because it has been previously shown that the deformation of the colliding drops play an important role in the drainage of the intervening gaseous film that prohibits coalescence, Yoon, et al. were interested in modeling the drop shape evolution throughout the collision process. They found that the drainage time of the film scales with $Ca^{4/3}$, where Ca is the capillary number. They also studied the relation between

the drainage time and the critical film thickness required for coalescence to occur. They found that at moderate Ca values, the internal circulation of the drop might actually arrest the drainage process, which implies there may be a critical Ca that is required for coalescence to occur. (Yoon, Baldessari, Cenicerros, & Leal, 2007)

Despite a rather extensive analytical and numerical investigation of the coalescence process, Yoon, et al. found a number of major discrepancies between the experimental results of past investigators and their own analytical results. For example, the experimental and analytically predicted drainage times varied significantly. The authors suggest some of the inconsistencies may be due to viscoelastic effects of the deforming surfaces that were unaccounted for, as well as the fact that the axisymmetric assumption used in the analysis may not be valid for moderate Ca values. In addition, they note that the continuum assumption may lose validity for sufficiently small film thicknesses. (Yoon, Baldessari, Cenicerros, & Leal, 2007)

Within the past year, investigators have continued to focus on improving existing numerical methods used in simulating drop-drop collisions. N. Nikolopoulos, et al. presented a numerical investigation using the Volume of Fluid scheme (V.O.F.), which is useful for tracking the

liquid-gas interface of the colliding drops (Nikolopoulos, Nikas, & Bergeles, 2009). They employed two separate V.O.F. indicator functions in order to track both colliding drops separately throughout the entire collision process. The authors compared their numerical results to the experimental results of Qian and Law (Qian & Law, 1997) and found that they agree very well. The V.O.F. method was able to accurately predict the details of the flow, such as the shape evolution of the colliding drops. Unfortunately, experimental data did not exist for very high We values, so the authors were unable to test their numerical scheme for collisions under such conditions.

Another recent numerical investigation of drop-drop collisions was performed by Shoaping Quan, et al. They used a three-dimensional moving mesh interface tracking method (M.M.I.T.) to simulate multiphase flows, such as those encountered during drop-drop collisions. They were able to accurately simulate the head-on coalescence of drop pairs by predicting the evolution of the bridge radius, which proved to agree well with experimental observations. (Quan, Lou, & Schmidt, 2009)

Investigations into the dynamics of drop-drop collisions continue to gain the interest of many investigators. Understanding the details of interactions between pairs or clusters of drops allows for the

possibility of manipulating individual drops precisely, which would be of great value to the study of microfluidics.

For example, a groundbreaking study was just recently published by Tristan Gilet and John W. M. Bush in which they investigated liquid drops falling onto a soap film. They considered two cases corresponding to a static soap film and a vibrating soap film. Under the static conditions, a number of collisions were observed, namely bouncing, crossing, where the liquid drop crossed through the soap film, and partial coalescence, where part of the approaching drop crossed the film and part of the drop was ejected from the surface as a satellite droplet. A theoretical analysis revealed that the soap film may be modeled as a non-linear spring. Through a combination of theoretical analysis and experimental investigation, the authors found that the critical Weber number that defines the transition between bouncing and crossing (crossing is analogous to coalescence in terms of drop-drop collisions) is $We_{crit} \sim 16$. (Gilet & Bush, 2009)

Chapter 2 Theoretical Models

2.1 PLANAR BODY APPROACHING NON-DEFORMABLE SURFACE

The situation of two liquid drops approaching one another may be viewed as a simple squeeze-flow problem, in which two bodies are brought together, forcing out the fluid between them. The "squeezing" of the intervening film causes a pressure distribution, which results in a normal force that is applied to each body. In order to gain a greater understanding of the physics involved with the collision of liquid drops, the problem may be further simplified by modeling the situation as a squeeze-flow involving two planar bodies: that is, a rectangular plate of mass m approaching a non-deformable, planar surface. A schematic of the problem description is shown in Figure 4.

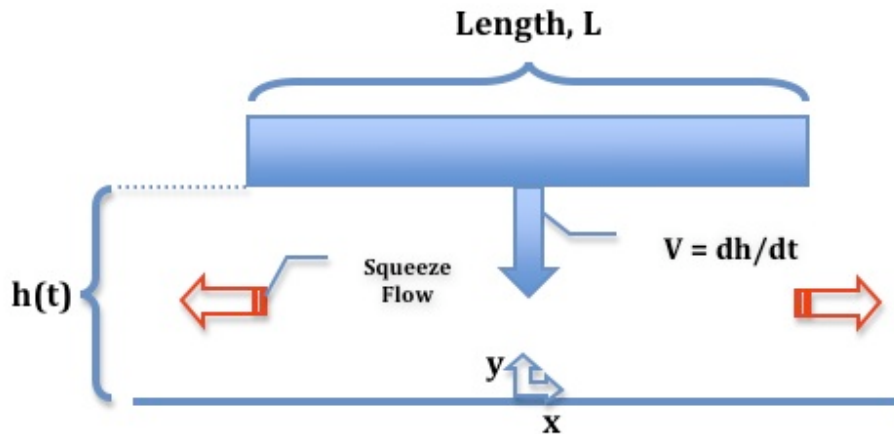


Figure 4: Squeeze-flow involving a planar body.

Squeeze-flow problems such as that described above typically involve flow regions where the characteristic length across the flow is very thin compared to the characteristic length *along* the flow direction (i.e. $h(t) \ll L$). If the corresponding Re of the flow is also small or moderate, lubrication theory may be utilized. This approximation is used throughout this analysis. It is also assumed that the intervening film is an immiscible fluid of constant density and that the flow is axisymmetric and unidirectional. In such a situation, an order-of-magnitude analysis applied to the conservation of momentum equation in the x -direction reveals that the inertia terms may be neglected, resulting in a balance between pressure and viscous forces (Panton, 2005):

$$0 = -\frac{dP}{dx} + \mu \frac{\partial^2 u}{\partial y^2} \quad (4)$$

A similar analysis of the y -direction conservation of momentum equation simply reveals that the pressure is dependent on the x position only, that is $P = P(x\text{-only})$.

The velocity profile of the intervening fluid is obtained by first integrating Equation (4) and applying the following boundary conditions:

$$u(y = 0) = 0$$

$$u(y = h) = 0.$$

The resulting velocity profile in the x-direction is

$$u(x) = \frac{y}{2\mu} \frac{dP}{dx} (y - h) \quad (5)$$

From the velocity profile, the volumetric flow rate of the intervening film, Q_{out} , is found to be

$$Q_{out} = 2w \int_{y=0}^h u dy \quad (6)$$

where w is the width of the approaching plate and the factor of 2 accounts for the symmetry of the unidirectional flow. A control volume analysis allows for the determination of the pressure distribution, which is achieved by equating the volumetric flow rate of the intervening film to the rate of change of the control volume. An appropriate control volume for this situation is shown in Figure 5.

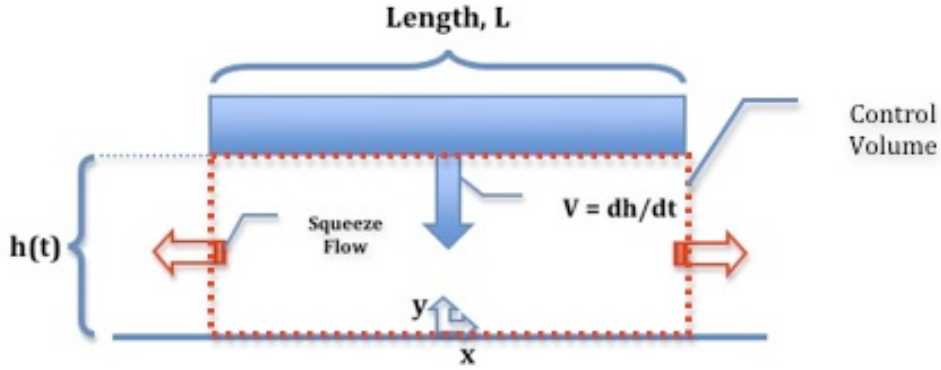


Figure 5: Control volume for squeeze-flow analysis.

The rate of change of the control volume is $2wx(dh/dt)$; continuity then requires that

$$2wx \frac{dh}{dt} = - \frac{wh^3}{6\mu} \frac{dP}{dx} \quad (7)$$

where the right-hand side of Equation (7) was obtained by evaluating the integral in Equation (6). Equation (7) may be rearranged to solve for the pressure gradient within the intervening film, which can then be used to obtain the pressure distribution throughout the film:

$$\begin{aligned} \frac{dP}{dx} &= - \frac{12x\mu}{h^3} \frac{dh}{dt}, \quad P(x = L/2) = P_0 \\ \therefore P(x) &= - \frac{3\mu L^2}{2h^3} h \left[\left(\frac{2x}{L} \right)^2 - 1 \right] + P_0 \end{aligned} \quad (8)$$

The single boundary condition needed to solve for the pressure distribution is the requirement that the pressure at the edge of the control volume be that of the ambient gas outside of the control volume, which is set equal to P_0 , or P_{atm} .

Finally, the hydrodynamic force acting upon the approaching bodies is obtained via integration of the pressure distribution, resulting in

$$F = \frac{w\mu L^3}{h^3} \dot{h} \quad (9)$$

The ultimate goal of this analysis is to obtain an evolution equation for the thickness of the intervening film. In terms of colliding drops, understanding how the intervening film diminishes in thickness and the corresponding surfaces deform would allow one to determine whether or not coalescence via attraction due to van der Waals forces is achievable under a given set of conditions. For the present case (i.e. a planar body approaching a non-deformable surface), application of Newton's law results in an evolution equation of the form:

$$F = ma = m \ddot{h} \Rightarrow \ddot{h} = \frac{w\mu L^3}{mh^3} \dot{h} \quad (10)$$

Nondimensionalization of governing equations is often very useful because it reduces the number of parameters that must be used to fully define a problem and it simplifies the governing equations significantly. In this case, the evolution equation given by Equation (10) may be nondimensionalized by introducing the following characteristic scales:

Characteristic length, $L_c = L$

Characteristic time, $t_c = m/(w\mu)$.

The resulting evolution equation for the nondimensional film thickness is

$$\ddot{\bar{h}} = \frac{\dot{\bar{h}}}{\bar{h}^3} \quad (11)$$

where the overbars represent nondimensional parameters. The present analysis may be extended to include bodies of various shapes approaching a non-deformable surface. The effect of the body shape on the evolution of the intervening film provides insight into the effect of surface deformation during a drop-drop collision. With this in mind, analyses were performed for both a disk-shaped body and a cylindrical body approaching a non-deformable surface (Figure 6).

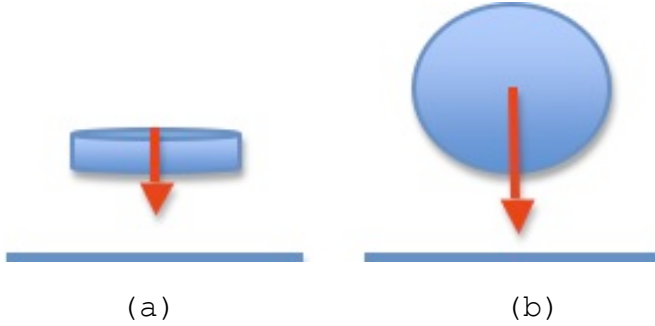


Figure 6: (a) Approach of disk-shaped body and (b) cylindrical body towards a non-deformable surface.

The derivations of the governing equations are identical in procedure (see Appendix A for complete derivations) to the planar case. The resulting evolution equations for the disk and cylindrical cases are:

$$\begin{aligned} \text{Disk : } \ddot{h} &= \frac{\dot{h}}{h^3} \\ \text{Cylinder : } \ddot{\delta} &= \frac{\dot{\delta}}{2} \frac{(2\bar{\delta} + 1)}{\bar{\delta}(\bar{\delta} + 1)^2} \end{aligned} \tag{12}$$

As shown, the cases of the disk and the plate approaching a non-deformable surface result in the same evolution equation for the intervening film thickness, h . The cylindrical body, however, results in a slightly more complex equation, indicating that indeed the shape of the approaching body affects the film thickness and hence the collision outcome.

2.2 PLANAR BODY APPROACHING DEFORMABLE SURFACE

The previous analyses involving various bodies of different shapes approaching a non-deformable surface may be expanded by allowing one surface to deform. This approach more closely simulates the drop collision process, since the drop surfaces deform as the pressure within the intervening film increases, which has been shown to have a significant effect on the collision outcome. The following schematic represents the setup of a squeeze-flow involving a planar body of length L approaching a deformable surface. This arrangement is very similar to that used in the analysis performed by Yiantsios and Davis (Yiantsios & Davis, On the Bouancy-Driven Motion of a Drop Towards a Rigid Surface or a Deformable Interface, 1990).

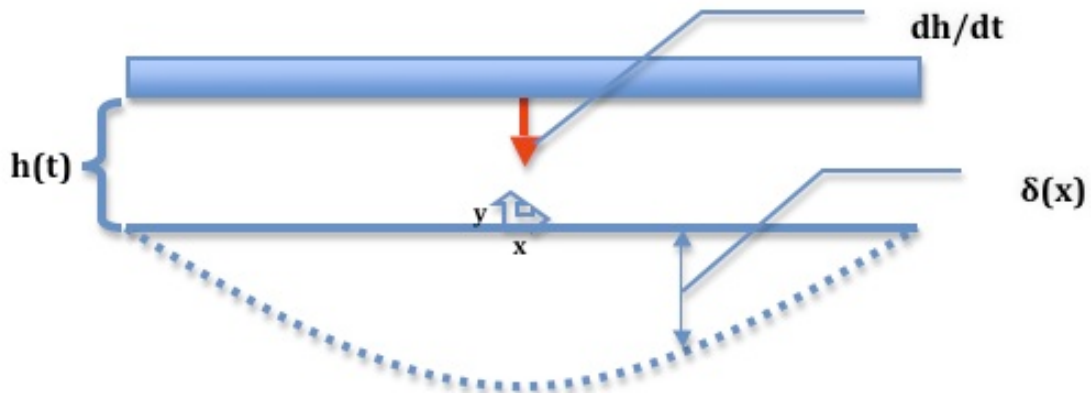


Figure 7: Squeeze-flow with deformable surface.

The procedure to obtain an evolution equation of the deformation, $\delta(x)$ for the situation shown in Figure 7 is identical to the previous cases involving non-deformable surfaces. Beginning with the simplified x-direction conservation of momentum equation (Equation (4)), the velocity profile of the film becomes

$$u(y) = \frac{P'}{2\mu} (-\delta y + \delta h + y^2 - hy) \quad (13)$$

The primary difference between the present analysis and that of the cases involving a non-deformable surface lies within the boundary conditions. With a deformable surface, the boundary conditions used to solve for the velocity profile are as follows: $u(h) = u(\delta) = 0$.

Once again, the volumetric flow rate of the film is obtained via integration of the velocity profile, that is

$$Q_{\text{out}} = 2 \int_{y=\delta}^h u \cdot w dy \quad (14)$$

Substituting the velocity profile into Equation (14) and performing the integration results in

$$Q_{\text{out}} = \frac{wP'}{\mu} \left[\frac{\delta h^2}{2} - \frac{h^3}{6} - \frac{\delta^2 h}{2} + \frac{\delta^3}{6} \right] \quad (15)$$

In this case, the control volume now includes a deformable surface. Therefore, the rate of change of the control volume is $wx(dh/dt - d\delta/dt)$, where the term $d\delta/dt$ accounts for the rate of change of the deformation of the deformable surface. As before, the volumetric flow rate of the film is set equal to the rate of change of the control volume, allowing an expression for the pressure gradient to be obtained:

$$P' = x\mu \left(\dot{h} - \dot{\delta} \right) \left[\frac{\delta h^2}{2} - \frac{h^3}{6} - \frac{\delta^2 h}{2} + \frac{\delta^3}{6} \right]^{-1} \quad (16)$$

Equation (16) shows that the pressure gradient is dependent on the position of the approaching plate as well as the deformation of the deformable surface. Because an exact form of the deformation is not known, an analytical solution is not available and numerical methods must be employed. In order to apply Newton's second law to the

approaching bodies, a finite-difference formulation is applied to the pressure gradient in Equation (16). This allows numerical integration to be used to solve for the force acting upon the approaching plate. Equation (16) may then be rewritten as

$$P^n = x\Delta x\mu\left(\dot{h}-\dot{\delta}\right)\left[\frac{\delta h^2}{2}-\frac{h^3}{6}-\frac{\delta^2 h}{2}+\frac{\delta^3}{6}\right]^{-1}+P^{n-1} \quad (17)$$

where the superscripts n and $(n-1)$ represent the nodal points along the x direction. Now, the force may be calculated by applying Newton's law and performing a numerical integration:

$$F = m\ddot{h} = 2w\sum_n P^n\Delta x \quad (18)$$

where the summation is carried out over the length $0\leq x\leq L/2$, and the factor of 2 accounts for the symmetry of the pressure distribution.

Finally, the governing equations are nondimensionalized with the following characteristic scales:

Characteristic length, $L_c = L$

Characteristic time, $t_c = m/(\mu w)$

Characteristic pressure, $P_c = \mu^2 w/m$

The resulting set of nondimensional governing equations becomes:

$$\begin{aligned} \ddot{\bar{h}} &= 2 \sum_n \bar{P}^n \Delta \bar{x} \\ \bar{P}^n &= \bar{x} \Delta \bar{x} \left(\dot{\bar{h}} - \dot{\bar{\delta}} \right) \left[\frac{\bar{\delta} \bar{h}^2}{2} - \frac{\bar{h}^3}{6} - \frac{\bar{\delta}^2 \bar{h}}{2} + \frac{\bar{\delta}^3}{6} \right]^{-1} + \bar{P}^{n-1} \end{aligned} \quad (19)$$

As shown in Equation (19), the pressure at each node is a function of the deformation at that particular node. Because the functional form of the deformation is not known explicitly, an additional parameter is needed to close the system of governing equations.

The pressure and deformation at each node may be linked by introducing the concept of Laplace pressure. The Laplace pressure refers to the overpressure that exists in the interior of a liquid drop, which is a result of the liquid's surface tension. Surface tension may be viewed in two perspectives; it may be viewed as the energy required to increase a surface area by one unit and it may also be viewed as a force per unit length, which acts normal to the surface and toward the liquid (de Gennes, Brochard-Wyart, & Quere, 2004).

A drop tends to adopt a spherical shape in order to reduce its surface area. When the surface area is increased, work is done by both the overpressure within the

drop as well as the surface tension. However, at mechanical equilibrium, the drop remains spherical and the pressure and capillary forces balance each other. This requirement is at the origin of Laplace's theorem, which states that the pressure difference across the surface of a drop is equal to the product of the surface tension and the curvature of the surface. In the present analysis, which is two-dimensional, only one curvature exists. Therefore, Laplace's theorem may be written mathematically as

$$\Delta P = P_0 - P = \frac{\sigma}{R} \quad (20)$$

The radius of curvature of an explicitly described curve with the form $y = f(x)$ is defined as (Edwards & Penney, 2002)

$$R = \frac{[1 + (y')^2]^{3/2}}{|y''|} \quad (21)$$

Therefore, Equation (21) may be used to define the radius of curvature of the deformable surface with the form $\delta = \delta(x)$ (Figure 7). Consequently, Equations (19)-(21) relate pressure to deformation, which allows for the deformation of the surface to be determined.

2.3 SYMMETRIC APPROACH OF TWO DEFORMABLE CYLINDRICAL BODIES

The analysis of a planar body approaching a deformable surface may be modified to model the situation shown in Figure 8.

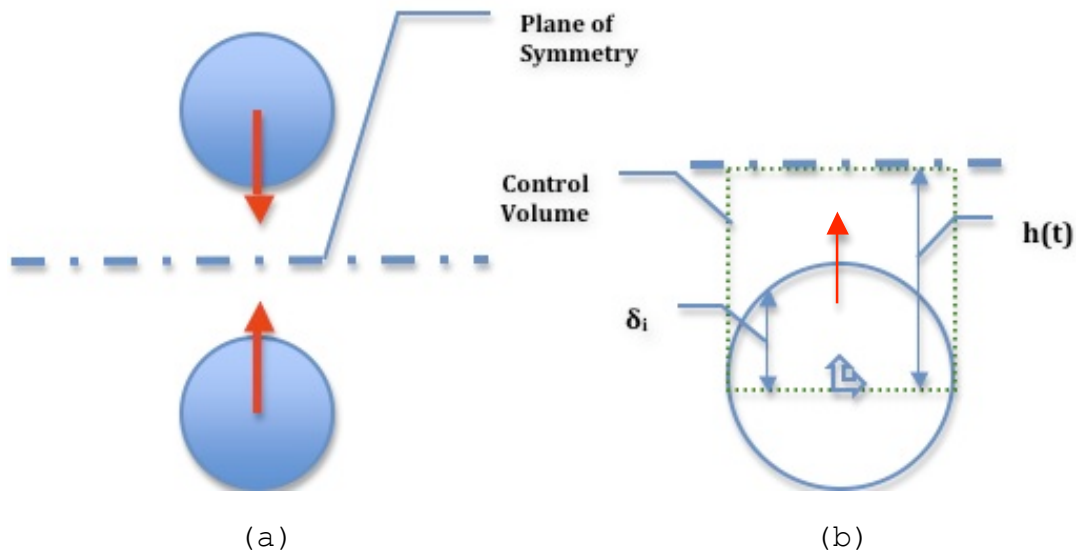


Figure 8: (a) Schematic of two liquid drops approaching one another (b) Appropriate control volume for current analysis.

Figure 8 illustrates a schematic of two liquid drops approaching one another (in two dimensions). Because of the symmetry of the flow within the intervening film, a plane of symmetry may be used to simplify the analysis. As a result, an appropriate control volume is that shown in Figure 8(b).

The control volume analysis for the situation depicted in Figure 8 is identical in procedure as the previous two analyses. However, it should be noted that in the current analysis a deformation is applied to the approaching bodies so that they are initially circular in shape, similar to actual liquid drops. As the bodies approach one another and the pressure within the intervening film increases, additional deformation will occur, causing the bodies to lose their circular shape (see Figure 9).

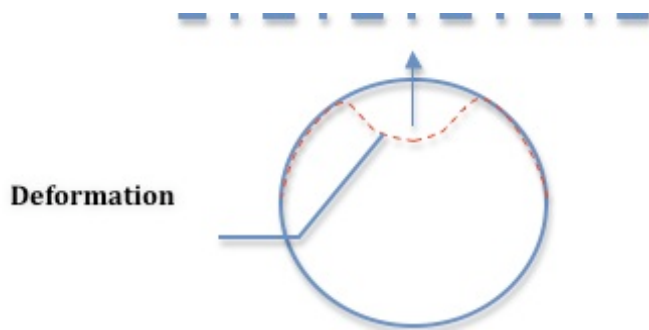


Figure 9: Example of surface deformation for initially circular body.

Once again, the simplified conservation of momentum equation in the x-direction is applied to the fluid flow within the intervening film. The boundary conditions for the velocity profile are:

$$\begin{aligned}\frac{\partial u}{\partial y_{y=h}} &= 0 \\ u(y = \delta) &= 0\end{aligned}\tag{22}$$

The first boundary condition is a symmetry condition that requires the velocity gradient along the plane of symmetry to be zero. The second boundary condition is simply a no-slip condition along the body surface. Application of these boundary conditions results in a velocity profile of

$$u(y) = \frac{P'}{2\mu} (y^2 - \delta^2) + \frac{hP'}{\mu} (\delta - y)\tag{23}$$

The volumetric flow rate is obtained in the same manner as before. The new limits of integration over which the velocity profile, $u(y)$ is integrated are $y = \delta$ (lower limit) and $y = h$ (upper limit). This accounts for the shape of the deformable surface, since the origin remains at the center of the approaching body. Again, by setting the volumetric flow rate of the film equal to the rate of change of the control volume, the pressure gradient of the film is found to be

$$P' = \frac{\dot{V}}{x} \mu \left(\dot{h} - \dot{\delta} \right) \left[\frac{(\delta^3 - h^3)}{3} - h\delta^2 + \delta h^2 \right]^{-1}\tag{24}$$

Following the same procedure as described in the previous section, the resulting set of governing equations is:

$$\begin{aligned}\ddot{\bar{h}} &= 2 \sum_n \bar{P}^n \Delta \bar{x} \\ \bar{P}^n &= \bar{x} \Delta \bar{x} \left(\dot{\bar{h}} - \dot{\bar{\delta}} \right) \left[\frac{(\bar{\delta}^3 - \bar{h}^3)}{3} - \bar{h} \bar{\delta}^2 + \bar{\delta} \bar{h}^2 \right]^{-1} + \bar{P}^{n-1} \\ \bar{R} &= \frac{\sigma}{P_c R_i (\bar{P} - \bar{P}_{in})}\end{aligned}\quad (25)$$

where P_c is the characteristic pressure scale ($P_c = \mu^2 w/m$), R_i is the initial radius of curvature of the cylindrical body, and P_{in} is the internal pressure of the cylindrical body. The initial internal pressure is defined by Laplace's equation (Equation (20)), where R_i is substituted for "R".

Chapter 3 Analogy to Mass-Spring-Damper System

3.1 VISCOELASTICITY AND THE MAXWELL MODEL

The outcome of a drop-drop collision is determined by the interaction between several mechanisms, namely the viscous damping of the drops' momentum by the intervening film, the deformation of the drops' surfaces due to surface tension effects, and the initial conditions of the drops as they are brought together. This complex system may be greatly simplified using a model of an analogous mass-spring-damper system (Figure 10).

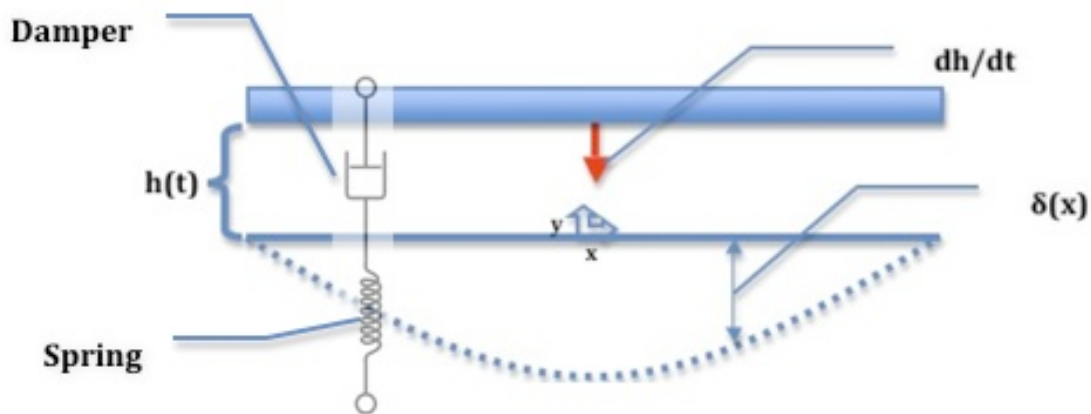


Figure 10: Analogy between fluidic system and mechanical mass-spring-damper system.

Figure 10 shows a mechanical mass-spring-damper system that is connected in series superimposed over the fluidic

system comprised of a planar body approaching a deformable surface. The implication is that as the mass approaches the deformable surface, the intervening film acts precisely as a viscous damper, slowing the plate's momentum by applying a normal force that opposes the plate's motion. The force also deforms the lower surface, which acts very much like a spring in that, as it deforms, it too applies a normal force that opposes motion. The interaction between these various mechanisms ultimately determines whether or not the plate will coalesce with the deformable surface, gradually come to rest at some position above the surface, or rebound due to sufficiently high damping forces.

The system of a spring element and damping element connected in series, such as that shown in Figure 10, is known as the Maxwell model. The Maxwell model is used to model viscoelastic materials, such as rubber, synthetic rubber-like materials, and commercial plastics. Viscoelastic materials are named as such simply because they exhibit both viscous and elastic behaviors when stressed.

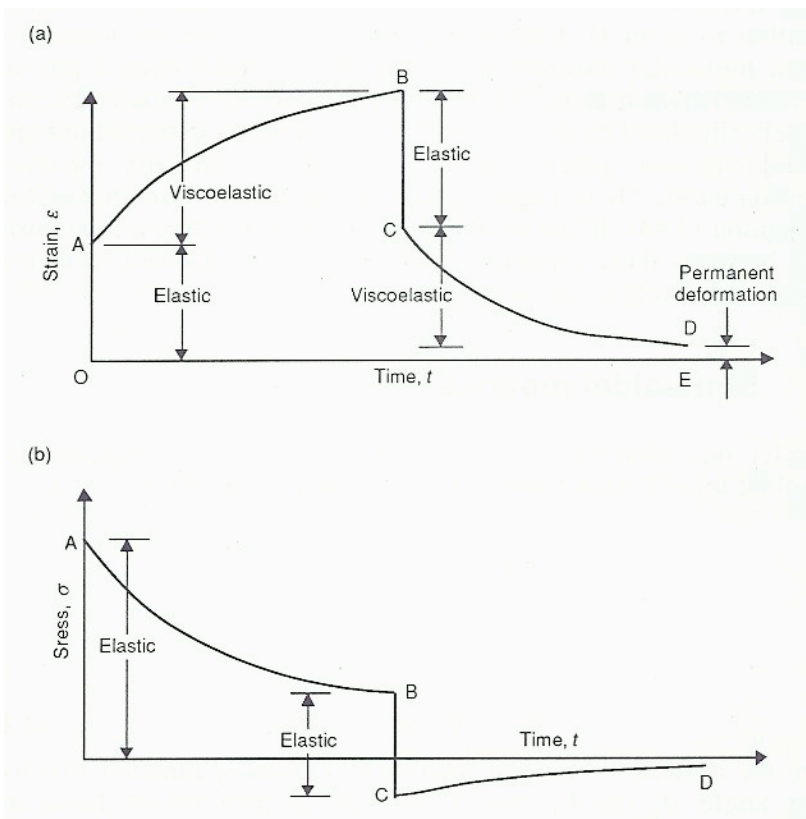


Figure 11: (a) Strain and (b) stress curves for a viscoelastic material. (Moore, 1993)

The defining characteristic of viscoelastic materials is demonstrated in the stress-strain curves presented in Figure 11. When a constant stress is applied to a viscoelastic material, it does not deform immediately but rather “creeps”, or flows over time. When the stress is removed, a viscoelastic material will hold some amount of residual deformation (Haddad, 1995). Because the system of two colliding drops contains both viscous-like and spring-

like elements interacting simultaneously, the Maxwell model with an attached mass should be an appropriate simplification.

3.2 TRANSFER FUNCTION ANALYSIS

A transfer function of a linear, time-invariant system of differential equations is simply the ratio of the Laplace transform of the output, or response function, to the Laplace transform of the input, or driving function. The purpose of a transfer function analysis is to represent a system of differential equations by a system of algebraic equations. By understanding the transfer function of a system, one can study the response under various forcing functions, which allows for a more thorough understanding of the nature of the system. (Ogata, 2004)

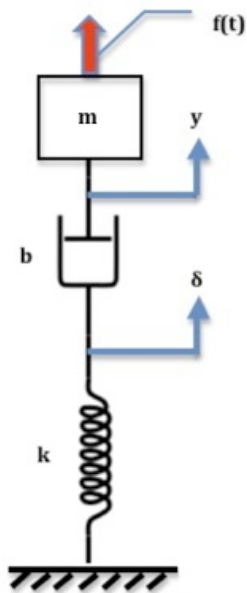


Figure 12: Mechanical mass-spring-damper system.

The system presented in Figure 12 is a mechanical mass-spring-damper system that is identical in form to the Maxwell model including an attached mass. The spring element has a spring constant k and the damper has a damping coefficient b . The system contains two nodes to be analyzed, with the responses of each node measured relative to their equilibrium positions.

The set of equations governing the motion of the mechanical system shown in Figure 12 is

$$\begin{aligned} m \ddot{y} &= -b(\dot{y} - \dot{\delta}) + f(t) \\ -k\delta - b(\dot{\delta} - \dot{y}) &= 0 \end{aligned} \tag{26}$$

Performing a Laplace transform analysis (see Appendix B for complete analysis) to Equation (26) results in a transfer function of

$$\frac{Y}{F} = \frac{bs + k}{mbs^3 + kms^2 + bks} \tag{27}$$

The highest power of s in the denominator of Equation (27) indicates that this system is a third-order system.

The denominator may be rewritten as $s(mbs^2+kms+bk)$, which reveals that the characteristic equation for the system is $(mbs^2+kms+bk) = 0$. The roots of the

characteristic equation determine whether the system will be underdamped, critically damped, or overdamped. The characteristic equation may be rewritten yet again as

$$s^2 + \frac{k}{b}s + \frac{k}{m} = s^2 + 2\zeta\omega_n s + \omega_n^2 \quad (28)$$

Equation (28) reveals that the natural frequency, ω_n of the system is $\sqrt{(k/m)}$ and the damping ratio, ζ is $\sqrt{(km)}/(2b)$. The damping ratio of this system, in which the spring and damper element are connected in series, is essentially the inverse of the damping ratio of the more common mechanical mass-spring-damper system in which the spring and damper elements are connected in parallel (i.e. $\zeta_{\text{parallel}} = b/(2\sqrt{(km)})$).

3.3 STATE-SPACE APPROACH AND DERIVATION OF SYSTEM PARAMETERS

The state-space approach was used to solve the system of differential equations that model the response of the mechanical mass-spring-damper system discussed previously (Equation (26)). The state-space representation is particularly useful for solving complex systems of equations because it allows a solution to be obtained very easily with use of a computer. State-space representations utilize both a state equation and an output equation so that the system may be represented by a vector/matrix. (Ogata, 2004)

Referring to Equation (26) and Figure 12, the state-space variables $x_1 - x_3$ are chosen to be:

$$x_1 = y$$

$$x_2 = dy/dt$$

$$x_3 = \delta.$$

Substitution of the selected state-space variables into Equation (26) results in the following system of equations:

$$\begin{aligned}\dot{x}_1 &= x_2 \\ \dot{x}_2 &= -\frac{b}{m} \left(x_2 - \dot{x}_3 \right) \\ \dot{x}_3 &= -\frac{k}{b} x_3 + x_2\end{aligned}\tag{29}$$

Like the sets of equations previously discussed, Equation (29) may be nondimensionalized by the following characteristic scales:

Characteristic length, $L_c = L$

Characteristic damping coefficient, $b_c = \sqrt{k}m$

Characteristic time, $t_c = \sqrt{m/k}$.

The resulting set of nondimensional equations is

$$\begin{aligned}\dot{\bar{x}}_1 &= \bar{x}_2 \\ \dot{\bar{x}}_2 &= -\bar{b}\left(\bar{x}_2 - \dot{\bar{x}}_3\right) \\ \dot{\bar{x}}_3 &= -\frac{1}{\bar{b}}\bar{x}_3 + \bar{x}_2\end{aligned}\tag{30}$$

In order to use the proposed mechanical mass-spring-damper system as a model for a fluidic system, such as that discussed in Section 2.2, an effective spring constant and damping coefficient is required. An effective spring constant may be defined as the ratio of a spring force to spring displacement, and an effective damping coefficient may be defined as the ratio of a damping force to the relative velocity of the damping element, that is

$$\begin{aligned}k &= \frac{F_s}{\delta} \\ b &= \frac{F_d}{\dot{\delta}}\end{aligned}\tag{31}$$

This very approach has been used to model elastomeric machine elements in terms of spring and damper elements (Moore, 1993).

Equation (16) may be used to determine a damping force for the fluidic system. Ignoring the spatial dependence of the position terms in the pressure gradient, a pressure distribution is found by integration:

$$P(x) = \int \frac{dP}{dx} dx = \frac{x^2}{2} \mu \left(\dot{h} - \dot{\delta} \right) \left[\frac{\delta h^2}{2} - \frac{h^3}{6} - \frac{\delta^2 h}{2} + \frac{\delta^3}{6} \right]^{-1} \quad (32)$$

The damping force may then be obtained by simply integrating the pressure distribution over the length of the entire plate. Symmetry is used to simplify the calculation:

$$F_d = 2 \int_{x=0}^{L/2} P(x) dA \quad (33)$$

where the differential area, $dA = (w)dx$. The resulting damping force is

$$F_d = \frac{w\mu L^3}{24} \left(\dot{h} - \dot{\delta} \right) \left[\frac{\delta h^2}{2} - \frac{h^3}{6} - \frac{\delta^2 h}{2} + \frac{\delta^3}{6} \right]^{-1} \quad (34)$$

Following Equation (31), the effective damping coefficient is found to be

$$b = \frac{w\mu L^3}{24} \left[\frac{\delta h^2}{2} - \frac{h^3}{6} - \frac{\delta^2 h}{2} + \frac{\delta^3}{6} \right]^{-1} \quad (35)$$

It should be noted that the velocity used in Equation (31) refers to the rate of change of the damping element, which in the case of the fluidic system is the rate of change of the film thickness. Therefore, the relative velocity $(dh/dt - d\delta/dt)$ was substituted for the term $d\delta/dt$ that appears in Equation (31).

Similarly, a dimensional analysis reveals that the effective spring constant, $k \propto \sigma_1$. The deformable surface acts most like a rectangular leaf spring, where the deformations and stresses are found by the equations governing the deflection of beams (Spotts, Shoup, & Hornberger, 2004). Therefore, the effective spring constant may be defined by $k = 48EI/L^3$, where E is Young's modulus, I is the moment of inertia, and L is the length of the surface. Young's modulus of a liquid drop is difficult to define; however, previous authors have taken E to be the Laplace pressure of the drop (Wang, Feng, & Zhao, 2008, Richard, Clanet, & Quere, 2002). This choice of adopting the Laplace pressure as an equivalent modulus of elasticity

may be rationalized by thinking of E as a "stiffness", or a resistance to deformation. When a compressive pressure is applied to a spherical drop, it is the overpressure that exists within the drop that resists the deformation. Further, because strain is a dimensionless parameter, Young's modulus has the units of pressure. For these reasons, the Laplace pressure is a natural choice for the effective modulus of elasticity of a liquid drop.



Figure 13: Schematic demonstrating similarity between cylindrical body and square beam approaching deformable surface, with the lubrication forces depicted as equivalent moments.

The moment of inertia, I , of a beam with cross-sectional area of $L \times t$ is defined as $wt^3/12$ (Spotts, Shoup, & Hornberger, 2004). However, the situation of a planar body approaching a deformable surface does not allow for

the direct calculation of I , since the thickness of the "beam", which in this case is the deformable surface, is non-existent. However, the situation of the approach and collision of two cylindrical bodies, which is the other fluidic model considered in this treatment, is very similar to the approach and collision of two beams with uniform cross-sectional areas (Figure 13). This situation allows one to calculate I , with the thickness of the beam, t , being equal to the length, L . Therefore, the moment of inertia is found to be $I = wL^3/12$. Substitution of E and I into the expression for k yields the following effective spring constant:

$$k = 4 \left(\frac{w}{L} \right) \sigma \quad (36)$$

The effective damping coefficient of the fluidic system given by Equation (35) is dependent upon the position of the approaching mass as well as the amount of deformation of the deformable surface, both of which are time-dependent. However, in order to apply the Laplace transform analysis and define an effective damping ratio, the mass-spring-damper system must be linear, meaning both the spring stiffness and the damping coefficient must be constant. To this end, a critical damping coefficient shall be defined.

Based on the form of the effective damping coefficient given by Equation (35), a critical damping coefficient may be defined as $b^* = \omega \mu L^3 / (24h^{*3})$, where h^* is a critical height of the approaching mass from the origin. Here, the complicated factor involving $h(t)$ and $\delta(t)$ in Equation (35) with dimension $[L]^3$ was replaced by a constant term h^{*3} . To define the value of h^* , a scaling analysis was performed.

A typical position trace of a mass approaching a deformable surface (see Section 2.2) is shown in Figure 14.

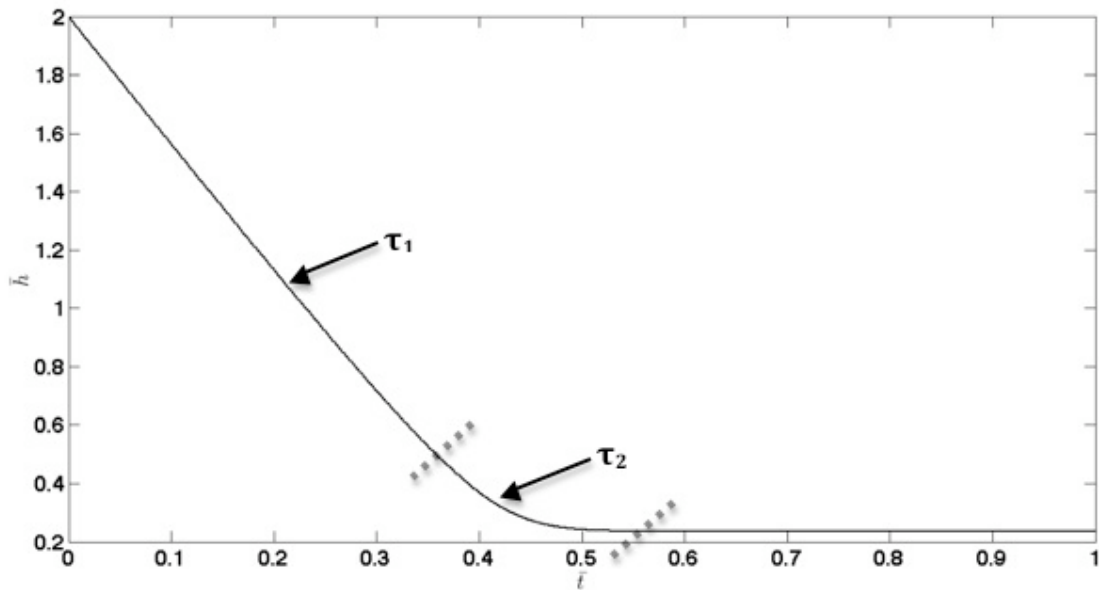


Figure 14: Typical position trace of fluidic system with various regimes labeled.

Regardless of the outcome of the approach, there exist two important regimes of differing characteristic time scales.

Initially, when the approaching body is far away from the deformable surface, the effective damping force, which is inversely proportional to h^3 , is essentially non-existent. This means the approaching body will experience no deceleration and will retain a constant velocity. This initial regime is denoted with the characteristic time τ_1 . Eventually, the approaching mass draws sufficiently close to the surface such that a damping force arises, which results in a deceleration as well as a deformation of the deformable surface. This regime has a different characteristic time than the previous regime, and it is denoted by τ_2 .

Because the initial regime of characteristic time τ_1 contains no deceleration of the approaching body, it is as if the two bodies are "unaware" of one another and nothing of physical significance occurs. Essentially, this initial regime may be disregarded in the present analysis. The regime that follows, however, is very important in the collision process. During this period when the approaching body experiences a damping force, all of the mechanisms that determine the ultimate outcome of the process (i.e. damping and deformation of the surface(s)) are provoked. Therefore, it is reasonable to conclude that both inertia and capillary effects are important in this regime. This fact was used to determine an appropriate value for h^* .

Newton's law may be applied to determine a characteristic time associated with the damping of the approaching body's momentum:

$$F_d = b^*V = ma = m \frac{dV}{dt} \quad (37)$$

The acceleration term, dV/dt in Equation (37) may be approximated by $\Delta V/\tau_2$. This leads to the conclusion that τ_2 , which may be referred to as τ_μ , is $\sim m/b^*$. It is important to note that b^* is used throughout this analysis, as opposed to simply b . The presence of b^* implies the use of h^* , which may be thought of as a critical height where both inertia and capillary effects are prominent. Hence, b^* is used in the determination of τ_μ . Substituting the form of b^* as defined previously, is it found that

$$\tau_\mu = \frac{24mh^{*3}}{w\mu L^3} \quad (38)$$

At this point, it remains to define h^* . The characteristic time associated with the damping of the approaching body, τ_μ , may be equated to a convective time scale within the region of interest; that is,

$$\tau_\mu = \frac{24mh^{*3}}{w\mu L^3} = \frac{h^*}{V_0} = \tau_{\text{conv}} \quad (39)$$

From Equation (39), $h^* = (w\mu L^3 / (24V_0m))^{1/2}$. Therefore, the resulting critical damping coefficient, b^* is

$$b^* = \frac{w\mu L^3}{24h^{*3}} = \frac{\sqrt{24}(V_0m)^{3/2}}{\sqrt{w\mu L^3}} \quad (40)$$

The critical damping coefficient given by Equation (40) is a constant value that is dependent only on system parameters and initial conditions, all of which are known quantities. Therefore, it may be used to define an effective damping ratio of the mechanical system, which was previously shown to be $\zeta = \sqrt{(km)/(2b)}$. Substitution of b^* yields the following effective damping ratio of the mechanical mass-spring-damper system:

$$\zeta^* = \frac{\sqrt{km}}{2b^*} = \frac{\sqrt{kw\mu L^3}}{2\sqrt{24mV_0}^{3/2}} \quad (41)$$

Chapter 4

Numerical Methodology

4.1 NUMERICAL METHODS AND PARAMETERS

All numerical computations were performed using Matlab® software (R2007a), with the aid of *Matlab®: An Introduction with Applications* (Gilat, 2005). The Runge-Kutta fourth-order procedure was used to obtain numerical solutions to the systems of ODEs. The Runge-Kutta methods eliminate the need for higher-order derivatives since they evaluate the sought function at more points than other methods (such as the Taylor methods) while maintaining sufficient accuracy. The truncation, or local error of the Runge-Kutta fourth-order method is $O(h^5)$ (Atkinson & Han, 2004).

All derivatives that appeared in the governing equations were approximated using first-order finite difference equations. The spatial and time resolutions of each program varied from one another. The time-step, dt of each program was dependent upon the initial conditions; that is, the time-step was defined by $dt = (h_0/V_0)/10,000$, where h_0 is the initial height of the approaching body ($h_0 = y_0$ for the mechanical m-s-d system), and V_0 is the initial approach velocity [m/s]. This condition ensured that the time resolution was sufficiently small compared to the

initial convective time scale. In all cases, the time-step was at *most* $dt_{\max} = 1e-3$.

Similarly, the space-step, dx was also dependent upon system parameters. For the two fluidic-system programs related to a non-deformable surface and a planar body approaching a deformable surface, the spatial resolution was such that precisely fifty nodes were generated. For the program that models two cylindrical bodies approaching one another, 500 nodes were used due to the additional complexity of the surface deformations. Because all the models were symmetric in space, this condition amounted to $dx = (L/2)/50$ (non-deformable and planar models) and $dx = (L/2)/500$ (non-planar with deformation model). The Matlab[®] codes used to generate the results presented herein can be found in Appendix C.

4.2 UNCERTAINTY ANALYSIS

Richardson extrapolation was used to determine an approximate uncertainty of the numerical results for each program. This method assumes that the error of an approximate solution is ch^P , where h is a parameter upon which the true solution $G(h)$ is dependent (for example, a time-step), and c and P are constants. The exponent P is known as the "rate" or "order of convergence", and an order of convergence of at least 1 implies the solutions are indeed convergent. (Kiusalaas, 2005)

A system of three equations of the form $G = g(h) + ch^P$, where h is varied each time, results in three unknowns that may be solved for, which allows a numerical error to be calculated. This method was applied to all four programs that were used to obtain the results presented in this treatment. The minimum position of the mass in each model was the parameter used to determine the error.

Table 1: Values of minimum position for various time-steps, dt .

Model	Timestep, dt		
	1.00E-03	5.00E-04	2.50E-04
Case A	0.485078737718828	0.485078737719026	0.485078737719041
Case C	0.463929106845121	0.464007317012150	0.464029271544826
Mechanical M-S-D	0.116371319590356	0.116373700302979	0.116374890637191
	4.00E-03	2.00E-03	1.00E-03
Case B	0.135475578369749	0.136322828206528	0.136421509366459

Table 1 lists the values of the minimum position of the approaching mass for each program (see Ch. 5 for description of each model) at three different time-steps (i.e. course, medium, and fine). It should be noted that Case B required a more course set of time-steps for this analysis. The data was then used to solve for the three unknowns of the previously discussed system of equations, which is shown in Table 2.

Table 2: Error analysis data.

Model	Order of Conv., P	C	G	% Error
Case A	3.723680	0.031762	0.485079	0.000000000044161%
Case C	1.832837	34.266711	0.464038	0.023431872972415%
Mechanical M-S-D	1.000027	0.004762	0.116376	0.004091336305245%
Case B	3.101941	26306.281668	0.135489	-0.688561470851335%

As shown in Table 2, the percent error for each program is well within an acceptable limit, with the highest error being approximately 0.7%.

Chapter 5 Results and Discussion

5.1 CASE A: PLANAR BODY APPROACHING NON-DEFORMABLE SURFACE

As discussed in Section 2.1, the collision of two liquid drops may be greatly simplified using a squeeze-flow model. The simplest such situation involves a planar body approaching a non-deformable, planar surface. The motivation behind analyzing such a simple model is the aspiration of gaining a firm understanding of the physics involved in a squeeze-flow problem. It has been shown that both a plate-shaped body and a disk-shaped body approaching a non-deformable surface result in the same set of governing equations. However, when the approaching body is given a cylindrical shape, the resulting set of governing equations differs from those of the plate and disk-shaped bodies. Figure 15 compares the position, velocity, and acceleration curves of the planar and non-planar (cylindrical) bodies under the same initial conditions. The system parameters used are as follows:

Length of plate, $L = 300e-6$ [m]

Width of plate, $w = 1000 \cdot L$ [m]

Radius of non-planar body, $R = L/2$ (= $150e-6$) [m]

Density of liquid, $\rho_1 = 1000$ [kg/m^3]

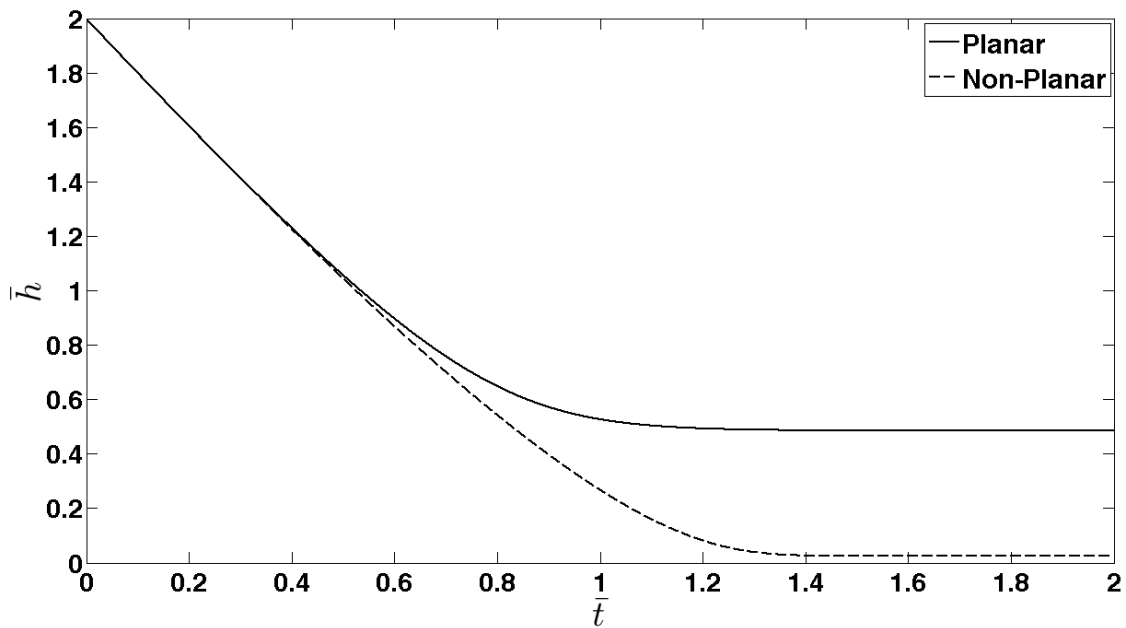
Viscosity of fluid film, $\mu_g = 1.79e-5$ [Ns/m^2]

Interfacial tension, $\sigma = 7.21\text{e-}2$ [N/m]

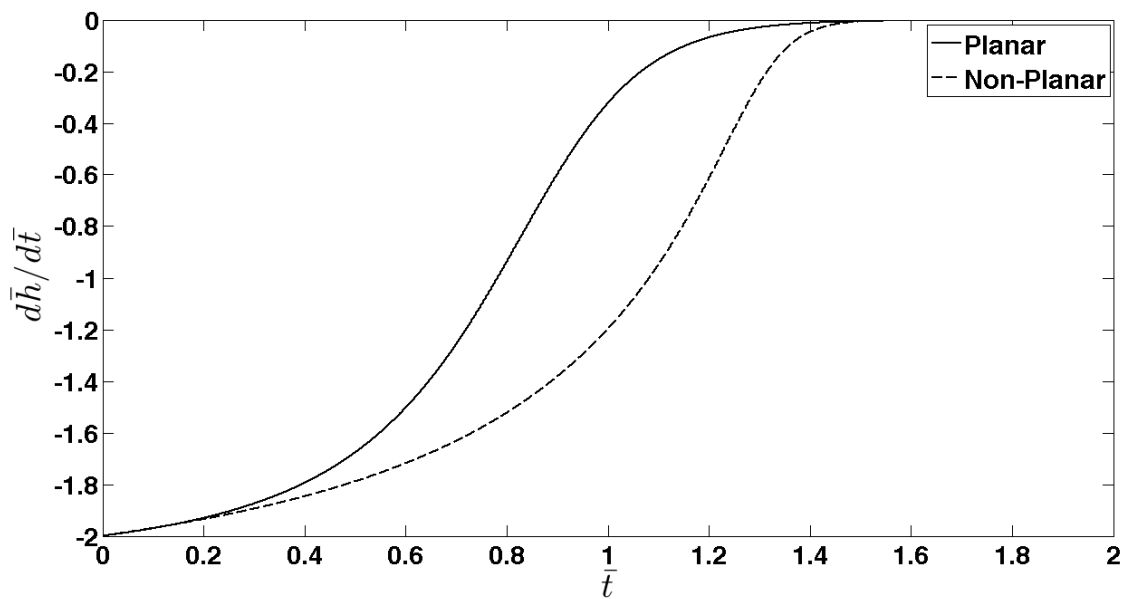
Ambient pressure, $P_0 = 101,325$ [Pa]

Mass of approaching body, $m = 4/3\pi(L/2)^3\rho_1$.

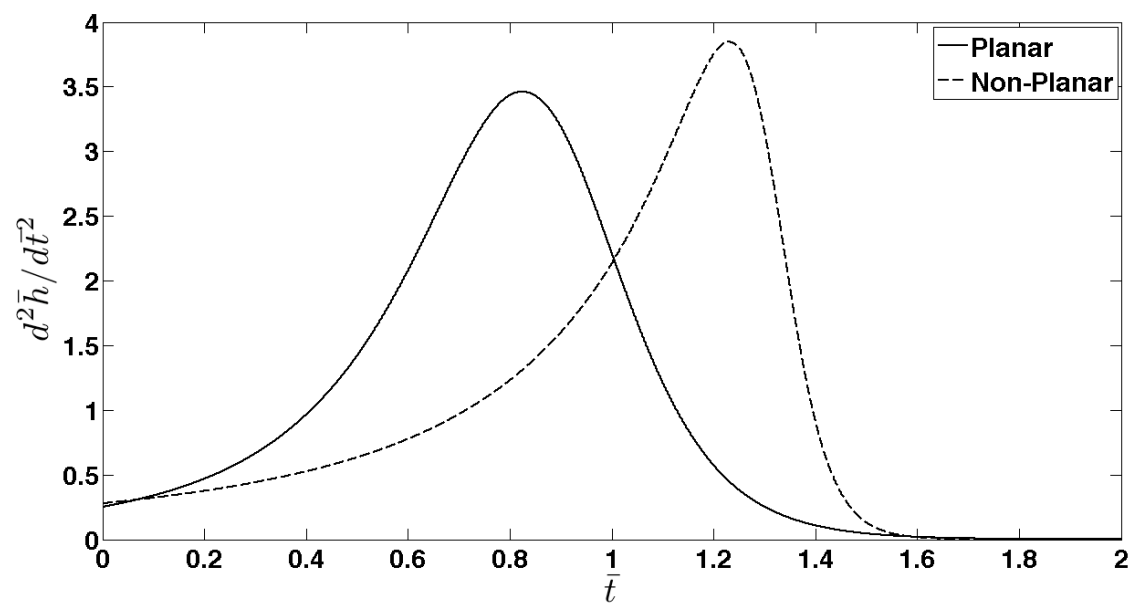
Unless specified otherwise, the above set of system parameters shall be taken as default values throughout the remainder of this treatment.



(a)



(b)



(c)

Figure 15: (a) Position traces of planar and non-planar bodies (b) Velocity comparison (c) Acceleration comparison.

As shown in Figure 15(a), the non-planar (cylindrical) body approaches the non-deformable surface much closer than the planar bodies. The velocity and acceleration curves show that the non-planar body experiences a slower deceleration, which allows the body to continue its approach for a longer period, resulting in a smaller minimum film thickness. These results indicate that not only does the shape of the approaching body affect the collision outcome, but also that a non-planar body will result in a smaller minimum film thickness. Although not presented here, the results of this particular setup are identical under all circumstances (i.e. neither rebound nor coalescence were observed).

The minimum film thickness is an important factor in determining whether coalescence will be achieved or not because the van der Waals forces are only significant at very small film thicknesses. Therefore, in order for the van der Waals forces to attract the approaching bodies together and cause coalescence, a minimum film thickness is required. For colliding drops, it has been shown that this value is $\sim 10^2 \text{ \AA}$ (Qian & Law, 1997).

It was mentioned in Chapter 2 that the lubrication approximation might be used to analyze squeeze-flow problems; however, this approximation has yet to be justified. The derivation of the governing equations for

the present analysis began with a simplified momentum equation. In order to employ such a simplification, the inertia terms of the Navier-Stokes equations must be neglected. Two conditions are required to satisfy this condition: a geometric condition and a dynamic condition.

The geometric condition necessary for application of lubrication theory is simply that the aspect ratio of the film, α ($= L_y/L_x$, where L_y and L_x are the length scales in the y and x directions, respectively) be much less than 1. This condition is easily met for all thin films and channel flows. The dynamic requirement for the lubrication theory is $Re_h\alpha \ll 1$. In other words, the product of the Reynolds number based on the film thickness and the film aspect ratio must be much less than 1. Figure 16 shows that although this dynamic condition is not met during the initial approach regime, the requirement is satisfied in the region where the approaching bodies are sufficiently close to one another. As discussed previously, it is in this regime where all the important mechanisms responsible for the collision outcome interact. Therefore, one may conclude that lubrication theory is valid within the region of interest for the present squeeze-flow analyses.

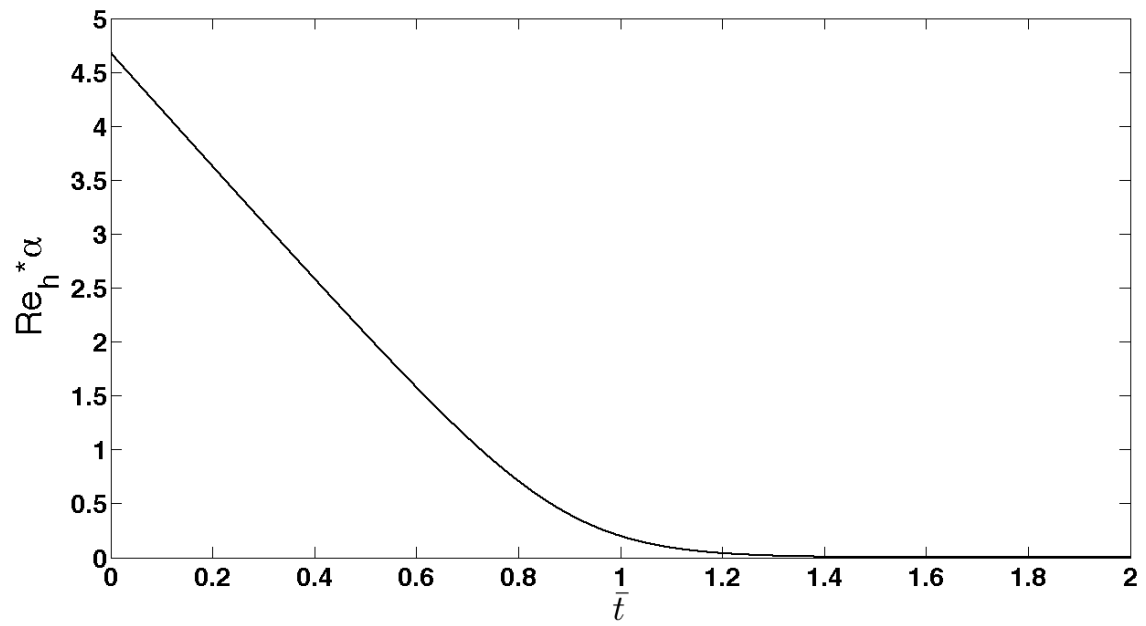


Figure 16: Dynamic condition for lubrication approximation.

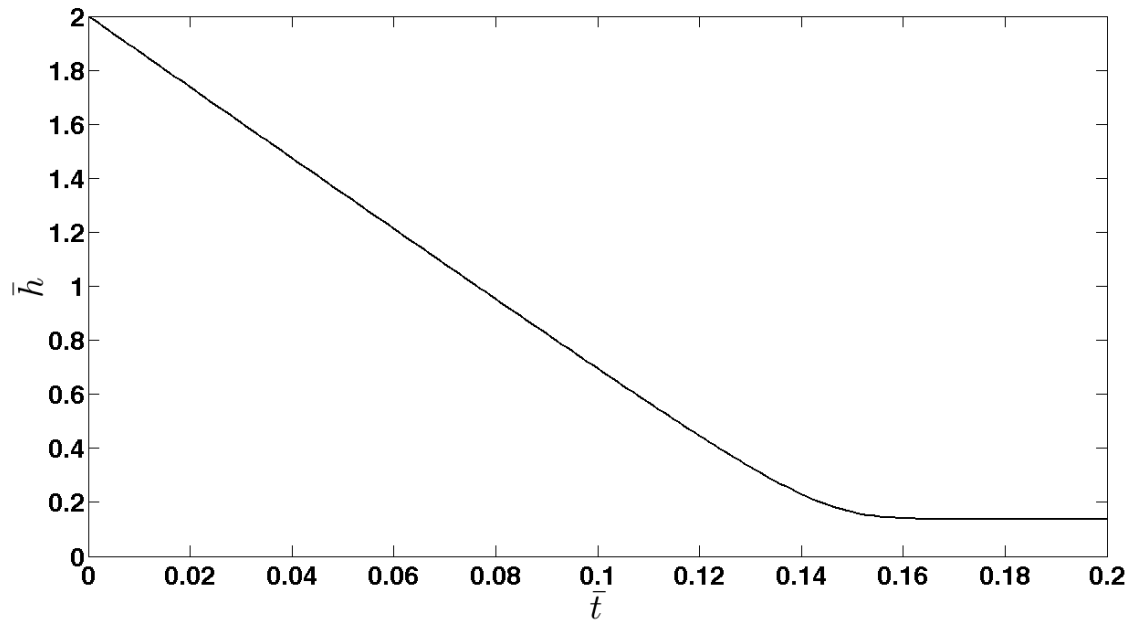
5.2 CASE B: PLANAR BODY APPROACHING DEFORMABLE SURFACE

A number of outcomes are possible when two drops collide, namely bouncing, coalescence, disruption, or fragmentation. The analysis of a planar body approaching a non-deformable surface revealed that under all circumstances the approaching body simply comes to a rest at some distance away from the surface it is approaching. The lack of deformation of either surface inhibits the possibility of bouncing to occur. In addition, the lack of deformation inhibits the drainage of the thin film that acts as a barrier to coalescence; as a result, coalescence is not observed under any circumstances. The analysis of a planar body approaching a deformable surface, however, shows that by allowing a surface to deform, "Rebound" is a possible outcome of the collision.

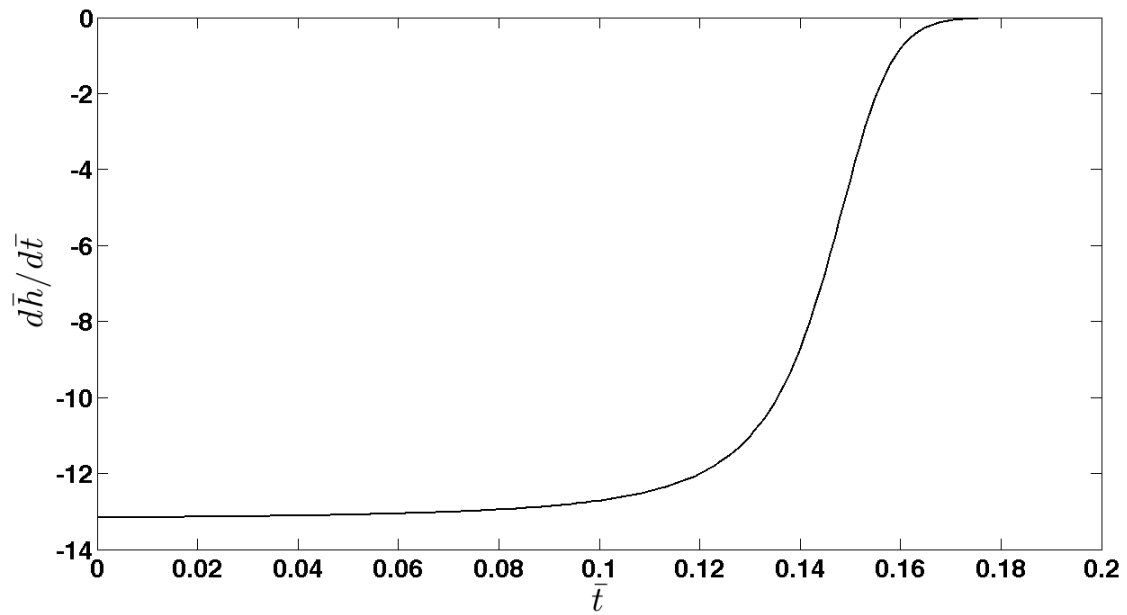
The governing equations used for the analysis of Case B are those that were derived in Section 2.2. In modeling Case B, the following criteria were used to define the outcomes of the collisions. The default outcome was set to "Rest", meaning that unless another outcome occurred throughout the collision process, the outcome would remain "Rest". This simply means that the approaching body came to a rest at some distance away from the deformable surface, which implies neither coalescence nor rebound

occurred. It is the author's opinion that in terms of an actual colliding-drop pair, "Rest" translates to a slow coalescence, an outcome that has been reported by a number of investigators (see Post & Abraham, 2002, Qian & Law, 1997). "Coalescence" was defined by the condition that the two bodies came within at least 400 Å from each other, the distance required for van der Waals forces to induce coalescence. This criteria is based upon the results of a number of studies as cited by Nikolopoulos, et al. (Nikolopoulos, Nikas, & Bergeles, 2009). Finally, "Rebound" was defined by the condition that the relative velocity between the approaching body and deformation of the deformable surface was such that the film thickness was increasing while the approaching body was bouncing away from the surface (i.e., the approaching body had a positive velocity) (note: all initial velocities are negative to account for direction of approach).

The following set of figures represent the results of a body approaching a deformable surface with an initial velocity of 1.5 m/s and default values for all other system parameters (see §5.1). It should be noted that this initial velocity, together with the set of default system parameters, corresponds to an effective damping ratio of $\zeta^* = 0.85$.



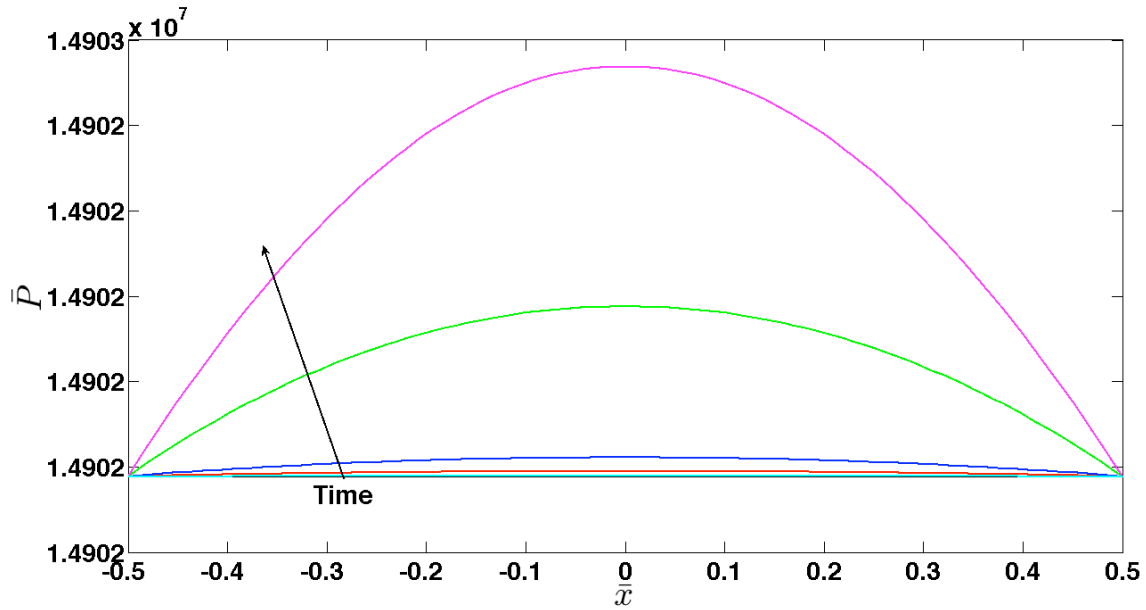
(a)



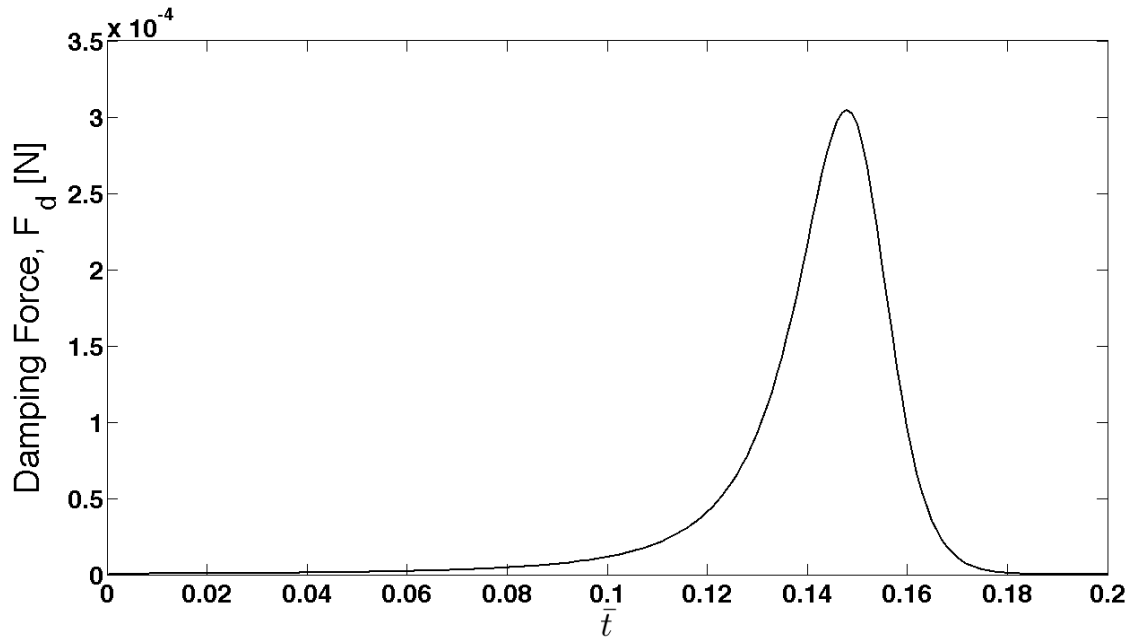
(b)

Figure 17: (a) Approach curve of body approaching deformable surface (b) Velocity trace of approaching body.

Figure 17 shows the approach and velocity traces of the approaching body. Under the initial approach velocity of 1.5 m/s, the body very gradually slows to a rest, which results in a non-dimensional minimum film thickness of approximately 0.2. This corresponds to a film thickness of $6e-5$ m, which is much greater than the required 400 \AA for coalescence ($400 \text{ \AA} = 4e-8 \text{ m}$). Therefore, the result of this particular collision is "Rest". Figure 18 shows the pressure distribution at various times throughout the collision process as well as the corresponding damping force trace.



(a)



(b)

Figure 18: (a) Pressure distributions over deformable surface at various times (b) Resulting damping force trace.

As shown in Figure 18(a), the pressure distribution within the intervening film maintains a parabolic form (see Equation (32)) as it increases in magnitude. Figure 18(b) shows the corresponding damping force, F_d [N] for the resulting pressure distributions. The damping force for this particular scenario reaches a maximum value of approximately $3e-4$ N, which is similar to values reported by previous investigators (see Bradley & Stow, 1978). Finally, the corresponding deformation of the deformable

surface at various times throughout the collision is shown in Figure 19.

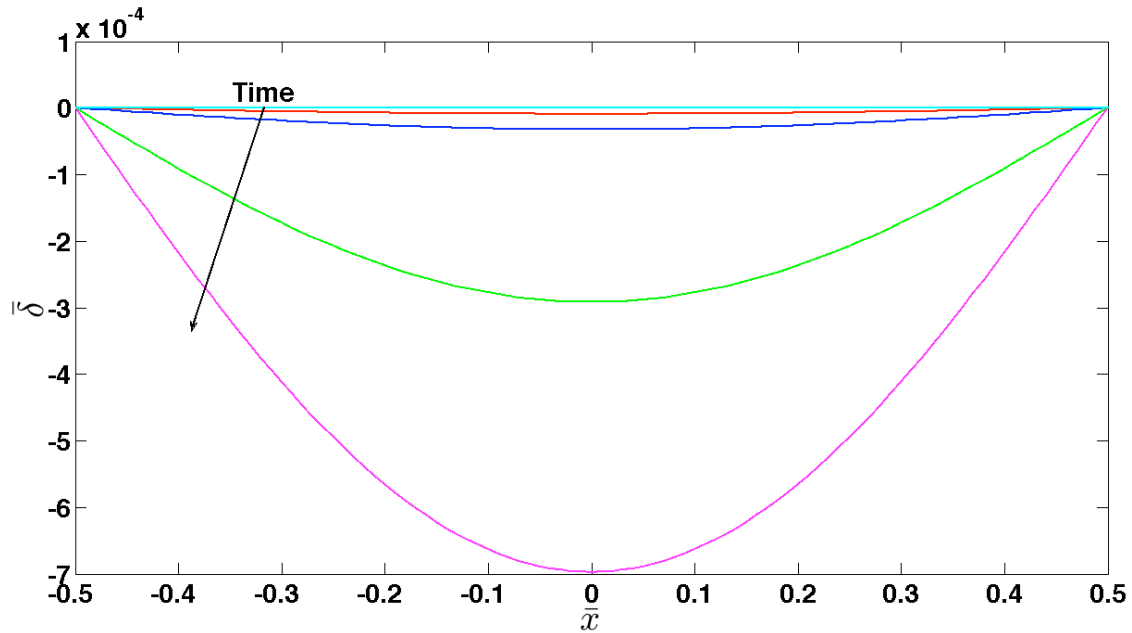
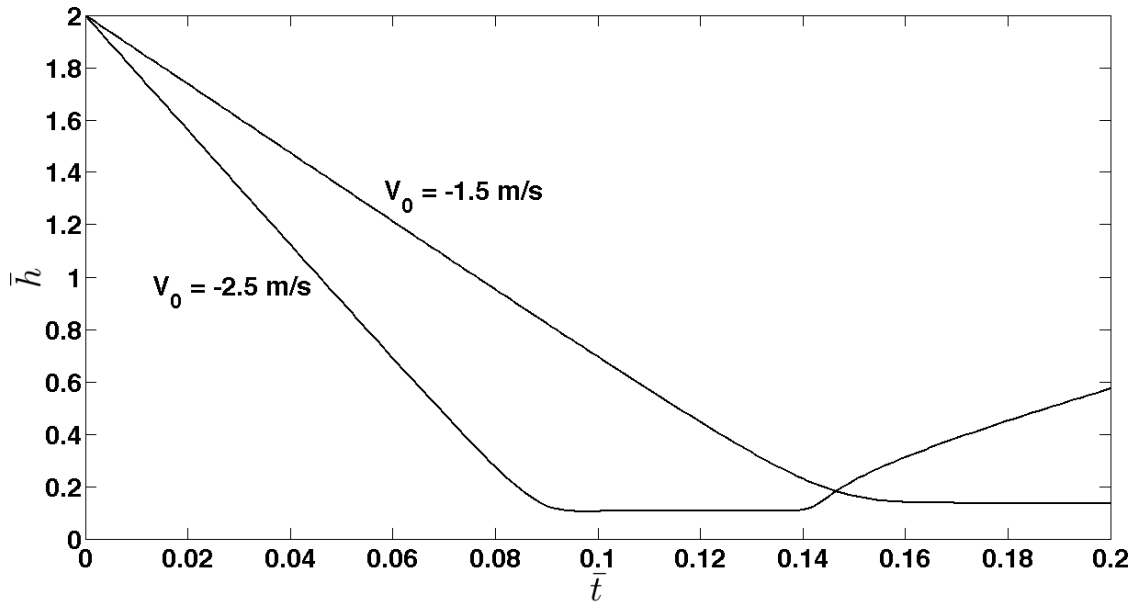


Figure 19: Deformation of deformable surface at various times throughout collision process.

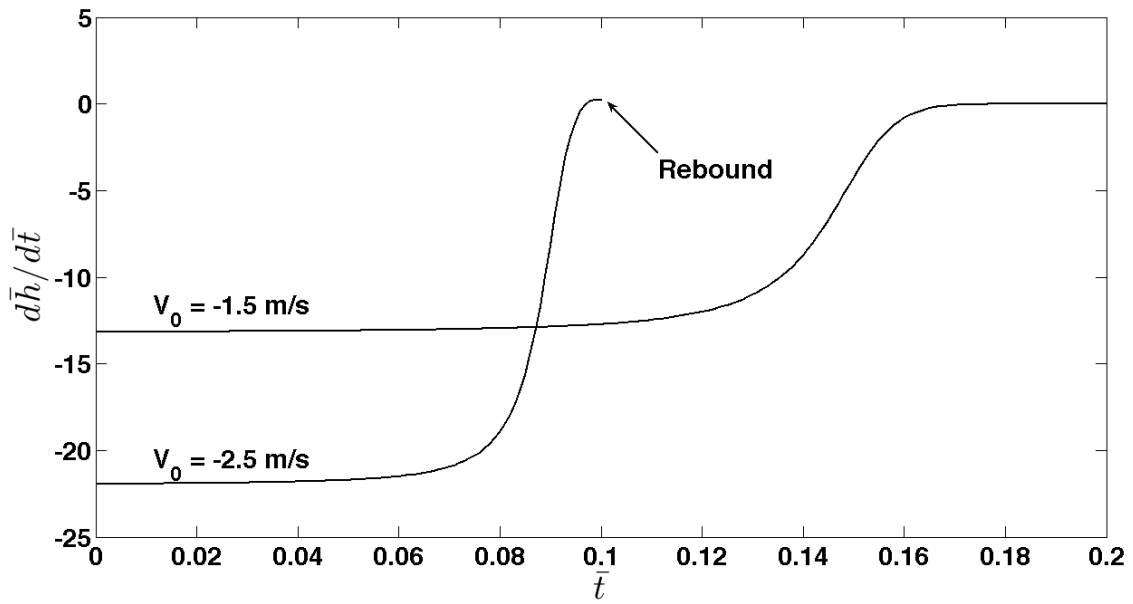
As expected, the deformation of the surface also maintains a parabolic form, similar to the corresponding pressure distributions. The maximum non-dimensional deformation is approximately $7e-4$, which corresponds to $2.1e-7$ m. This value is much smaller than the characteristic length of the problem, L_c . Therefore, this deformation should be considered minor, which may help explain the outcome of the collision. For minor deformations, it is expected that the spring effect of the deforming surface will also be minor,

which results in a situation that closely resembles that of Case A. As shown in Section 5.1, the scenario of a planar body approaching a non-deformable surface (Case A) results in nothing other than "Rest". Therefore, for minor deformations, it is reasonable to conclude that rebounding cannot occur. Furthermore, one may conclude from these results that surface deformation is indeed critical to the collision outcome.

The result of the collision changes significantly with an increased approach velocity of 2.5 m/s, which corresponds to an effective damping ratio of 0.40. The approach curve and velocity trace for this situation as compared to the previous case of $V_0 = 1.5$ m/s is shown in Figure 20.



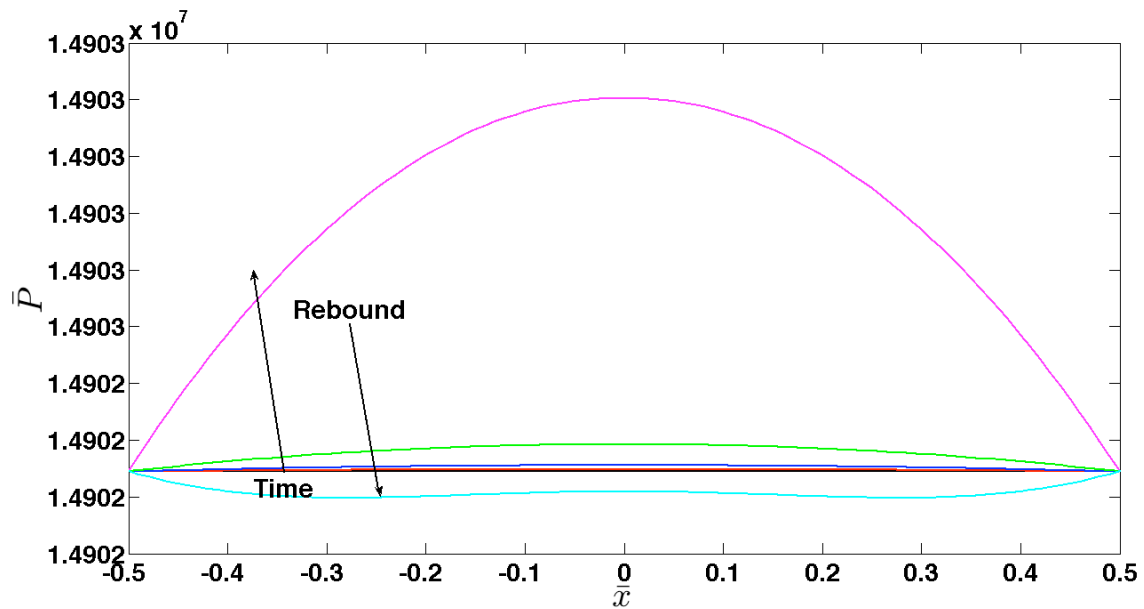
(a)



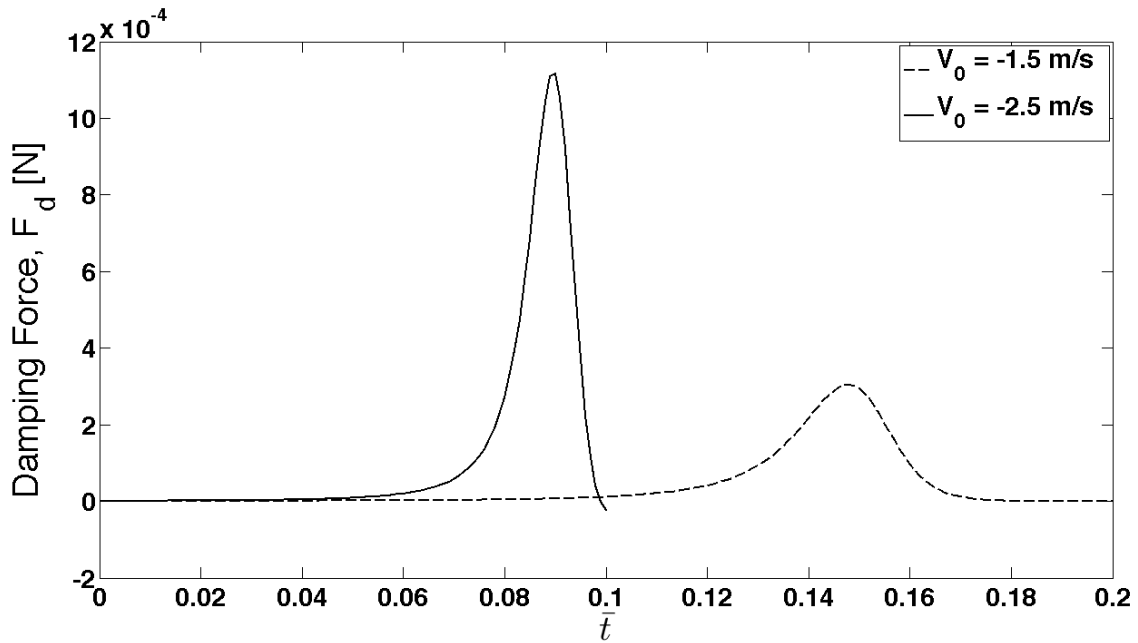
(b)

Figure 20: (a) Comparison of position traces for two different approach velocities (b) Comparison of velocity traces for two different initial approach velocities.

As shown, a higher initial approach velocity of 2.5 m/s results in the approaching body rebounding away from the deformable surface rather than simply slowing to a rest. As expected, the increased momentum of the body at the start of its approach results in a smaller minimum film thickness as well as a faster collision time, meaning the body decelerates at a higher rate. Figure 21 shows the pressure distribution over the deformable surface at various times throughout the process as well as the corresponding damping force for both approach velocities.



(a)



(b)

Figure 21: (a) Pressure distributions over deformable surface at various times (b) Comparison of damping force trace for two different approach velocities.

The pressure distributions are very similar in form for both initial approach velocities. The damping force, however, is much larger for the higher approach velocity; the maximum force is approximately three times that of the previous case. In addition, for the higher initial approach velocity of 2.5 m/s, the outcome of the collision is "Rebound". As shown in Figure 21(a), the value of the pressure across the deformable surface becomes less than ambient pressure, which implies the occurrence of a suction effect. Previous investigators have shown that coalescence

of colliding drops occurs during the rebounding phase of the process as opposed to the initial approach (Bremond, Thiam, & Bibette, 2008). The resulting low pressure that occurs within the intervening film due to the rebound causes the formation of "nipples" along the surface, which serve to induce coalescence by bringing the corresponding surfaces close enough for van der Waals forces to act.

The deformation of the surface at various times throughout the collision is shown in Figure 22.

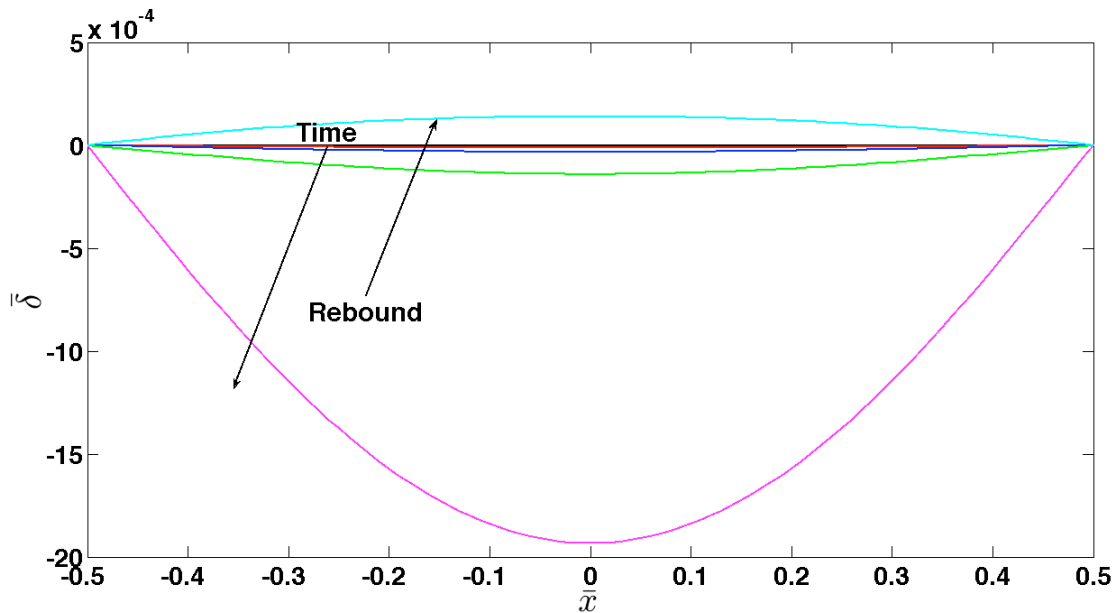


Figure 22: Deformation of deformable surface at various times throughout collision process for initial approach velocity of 2.5 m/s.

It is shown in Figure 22 that the deformable surface does indeed experience suction at the time of rebound, which is evident by the positive deformation. It should also be noted that the maximum deformation is much larger than that for the previous case of $V_0 = 1.5$ m/s. The greater deformation translates to a greater spring effect, which promotes rebound.

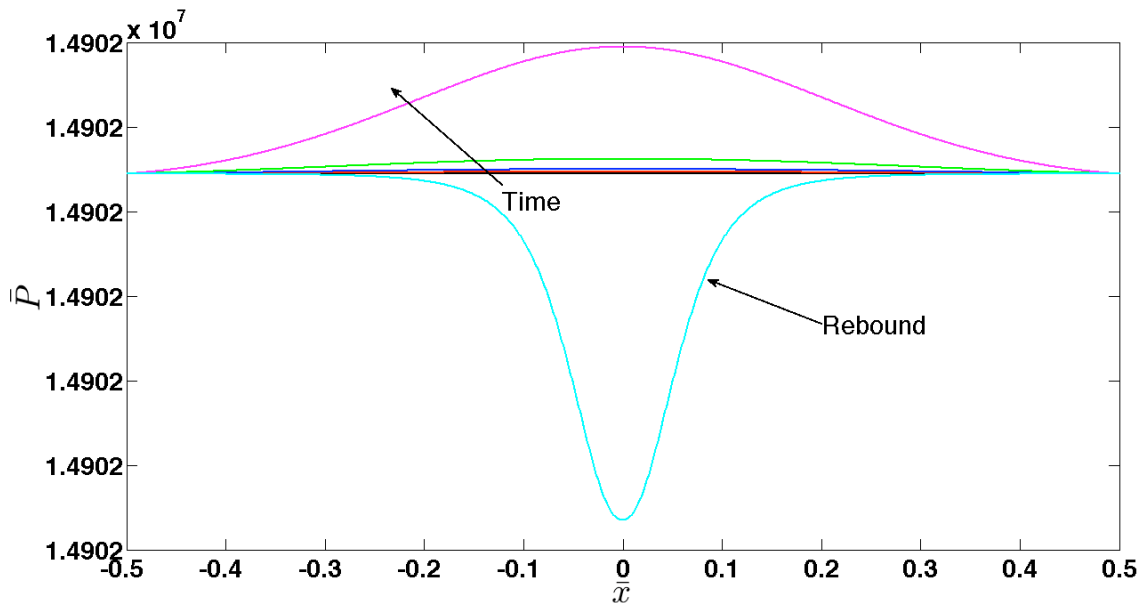
Although rebound and suction occur, coalescence is not observed under any circumstances when modeling a flat plate approaching a deformable surface. This is most likely

because of the initial, non-deformed geometry, which inhibits the formation of a "nipple" on the surface. This observation serves as the motivation for extending the study to model two cylindrical bodies approaching one another, while allowing deformation of both surfaces (see §2.3). This type of model allows for the possibility of the formation of two "nipples" during the separation phase of the collision, which may serve to bring the surfaces close enough to merge via van der Waals attraction (Bremond, Thiam, & Bibette, 2008).

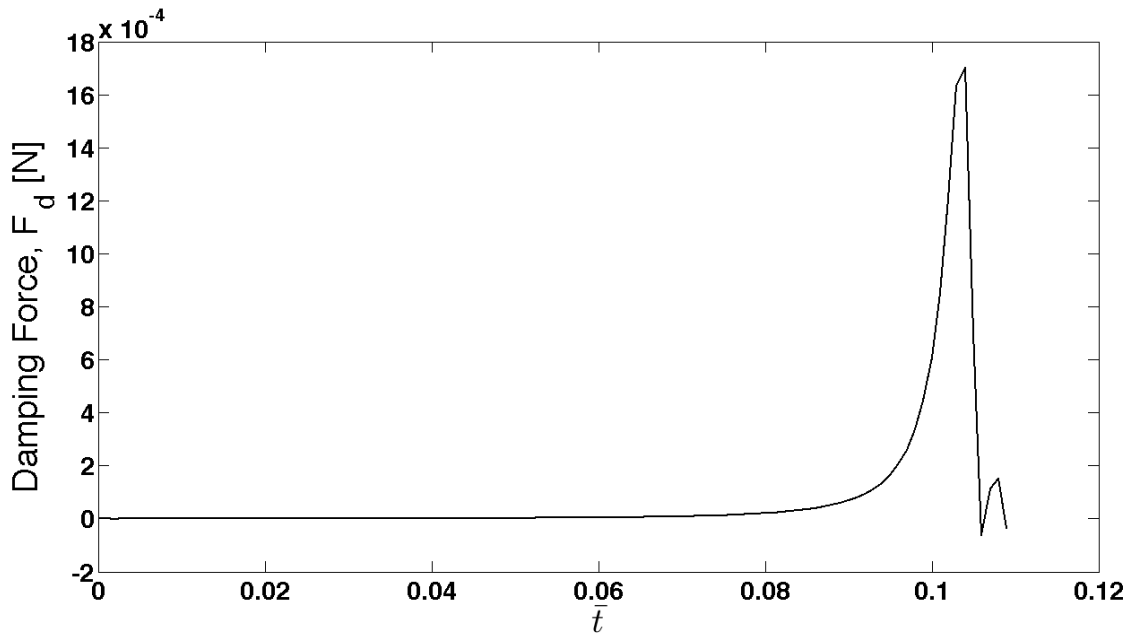
5.3 CASE C: SYMMETRIC APPROACH OF TWO DEFORMABLE CYLINDRICAL BODIES

As previously discussed, the symmetric approach of two cylindrical bodies with deformable surfaces is modeled to more closely approximate the approach and collision of two spherical drops while maintaining the necessary requirements for the unidirectional flow approximation. The results of this particular model are very similar to those of Case B; however, the initial circular geometry allows coalescence to occur during the rebound phase of the collision.

The following figures represent the results for a relative approach velocity of 1.75 m/s ($\zeta^* = 0.95$).



(a)

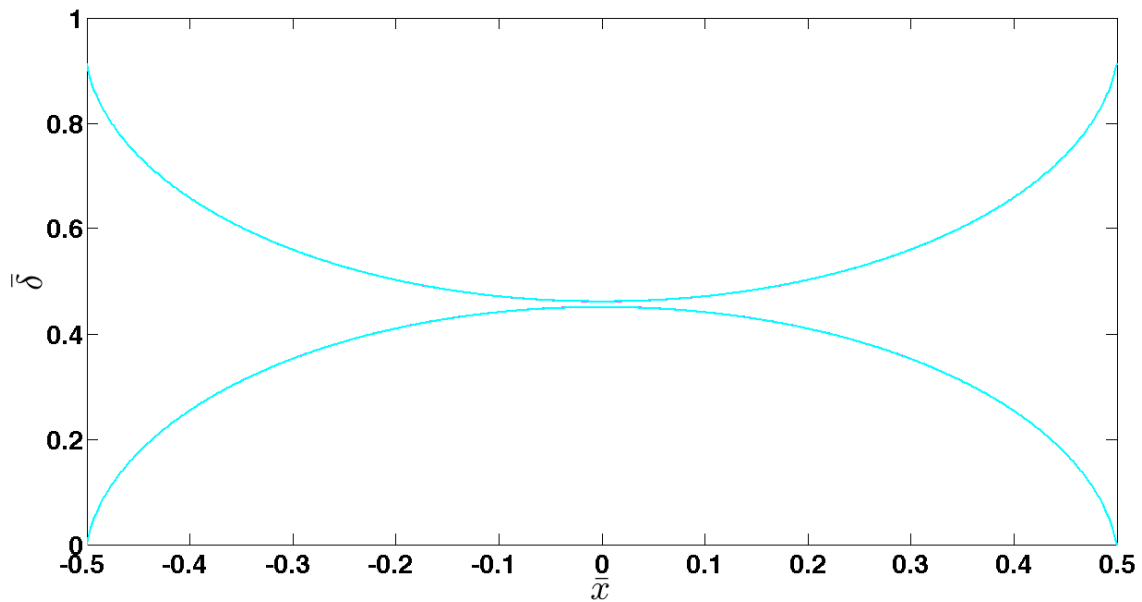


(b)

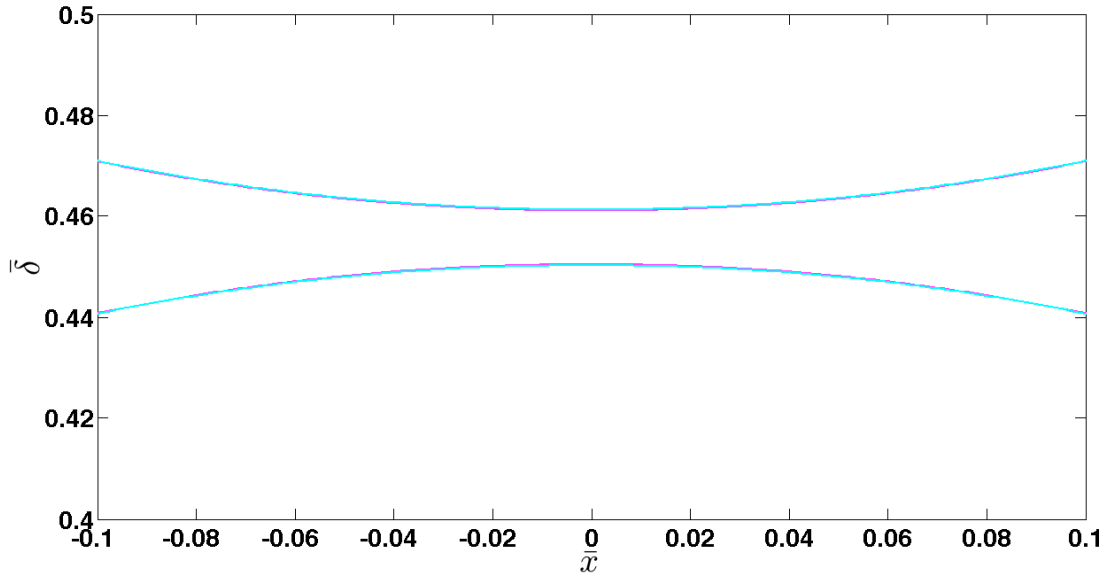
Figure 23: (a) Pressure distribution within intervening film at various times (b) Trace of corresponding damping force.

For a moderate approach velocity, the two cylindrical bodies experience rebound without coalescence. As shown in Figure 23(a), the pressure distribution at various times throughout the collision process is very different in form when compared to the previous case of a planar body approaching a deformable surface. A suction effect is evident for the present case; however, the low pressure within the intervening film that results from the rebound is significantly lower than that for Case B. This is due to the initial geometry of the approaching bodies. Because

of the circular shape, the initial film shape is similar to a converging-diverging nozzle, as shown in Figure 24. Therefore, it should be expected that the pressure at the center of the film would be much lower than elsewhere along the film region. This low pressure is intensified upon rebound. The suction is also evident in the damping force, where the sign changes at the point where the bodies are sucked back toward each other, indicating a change in direction of motion.



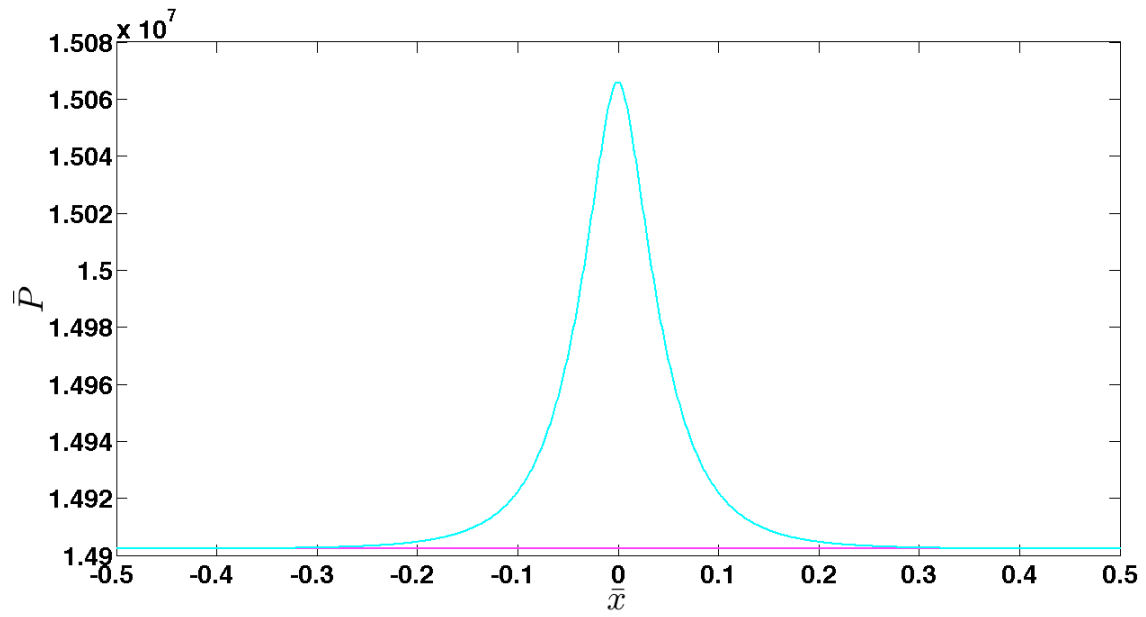
(a)



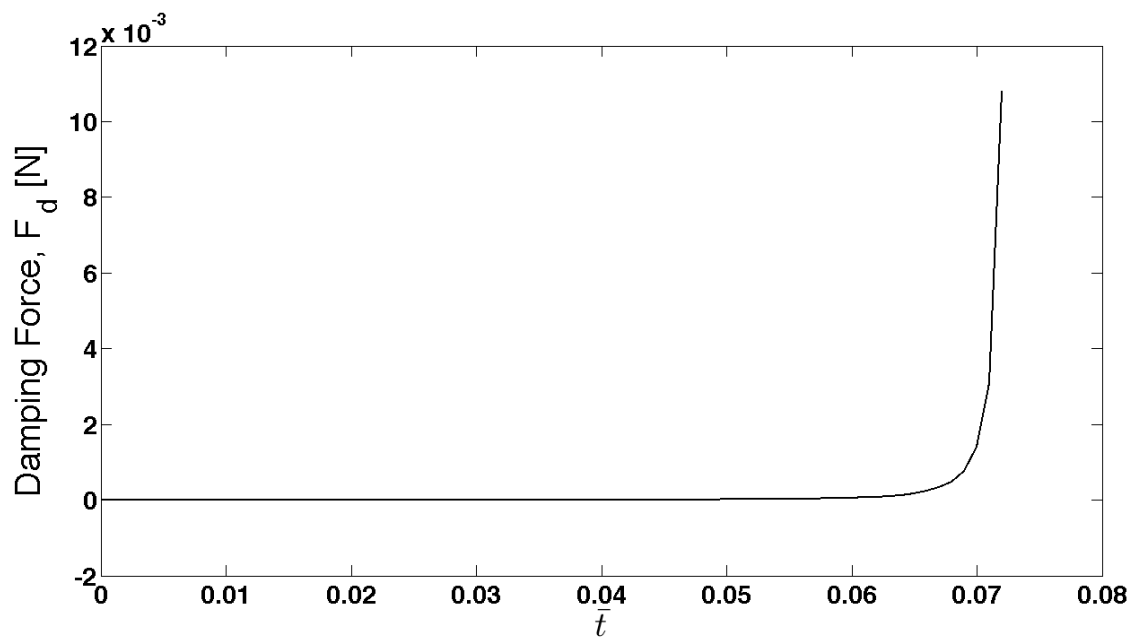
(b)

Figure 24: Shape of intervening film upon rebound for two approaching cylindrical bodies (b) Magnified view of film shape.

At a higher relative approach velocity of 2.5 m/s ($\zeta^* = 0.56$), coalescence is observed upon rebound. The higher momentum results in a transfer of more surface energy, which relates to a stronger spring effect and hence a stronger suction. This suction is sufficiently strong such that dimples are formed on the surfaces of the approaching bodies, which allow the interfaces to connect. The pressure distribution at various times and the corresponding damping force for this situation are shown in Figure 25.



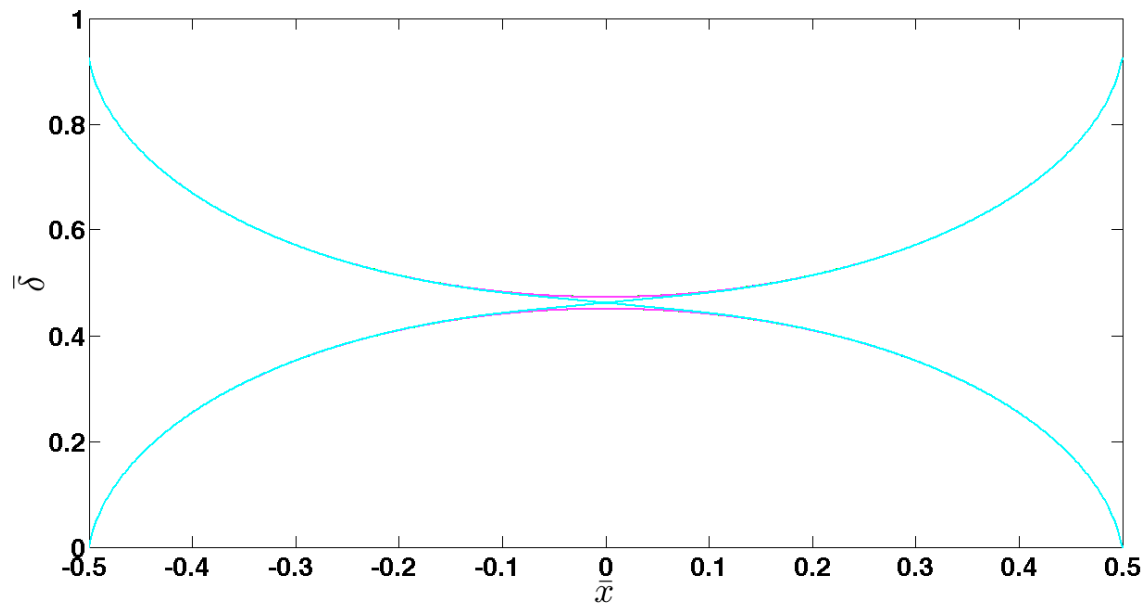
(a)



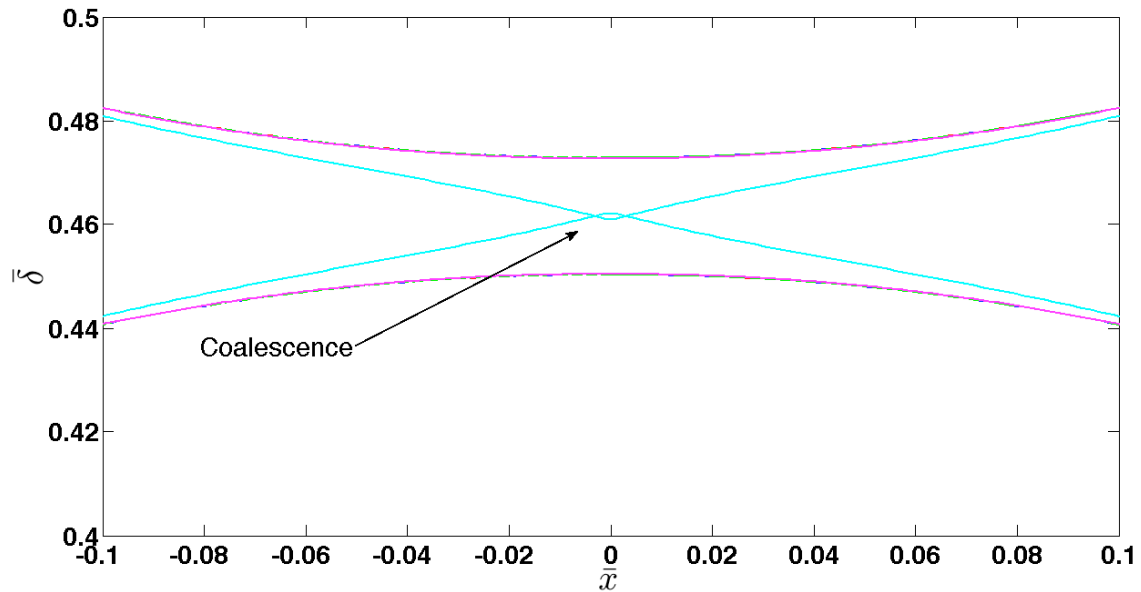
(b)

Figure 25: (a) Pressure distribution at various times throughout collision process (b) Corresponding damping force trace.

Because coalescence was induced, the suction effect is not evident in Figure 25. It should be noted, however, that both the pressure and damping force are much higher than the previous values corresponding to the lower approach velocity of 1.75 m/s. More interesting is the shape of the intervening film during the collision process.



(a)



(b)

Figure 26: (a) Shape of intervening film during coalescence of approaching bodies (b) Magnified view of film during coalescence.

Figure 26 clearly shows the formation of “nipples” on the surfaces of both interfaces. The formation of the “nipples” creates a region where the intervening film is completely drained and the interfaces are capable of merging. The possibility of coalescence is the primary difference between the model of a planar body approaching a deformable surface and the symmetric approach of two, cylindrical bodies, both with deformable surfaces. However, the critical system parameters that define the transition between “Rest” and “Rebound”/“Coalescence” are

very similar for both models, a result that is discussed in more detail in the next section.

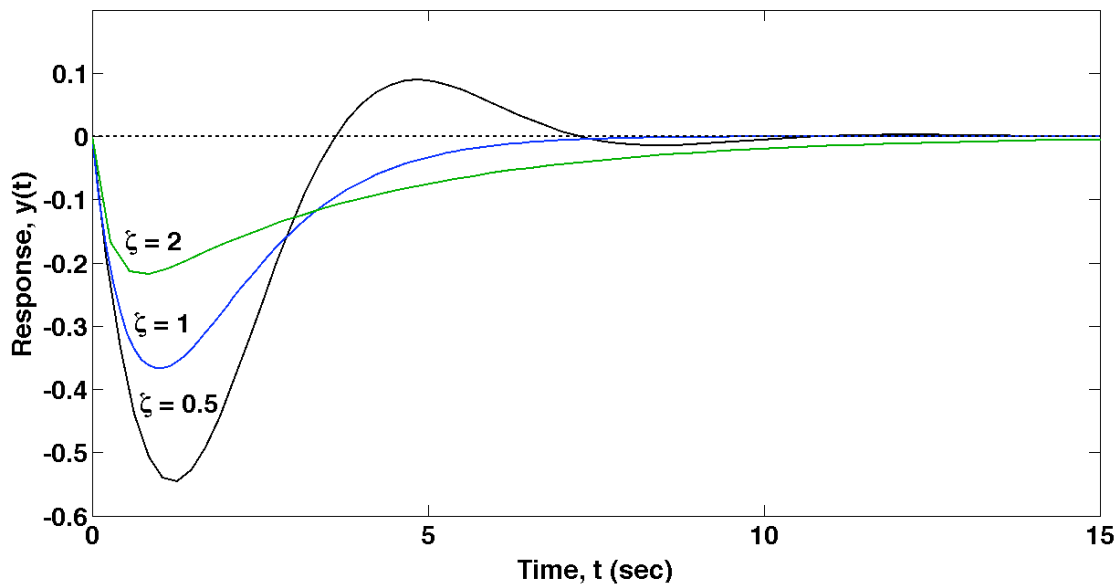
5.4 COMPARISON BETWEEN FLUIDIC MODELS AND ANALOGOUS MASS-SPRING-DAMPER SYSTEM

As discussed in Chapter 3, the fluidic systems that represent the approach and collision of two liquid drops may be modeled by a mechanical mass-spring-damper system. It has been shown that a Maxwell model with an attached mass very closely resembles the collision of two liquid drops.

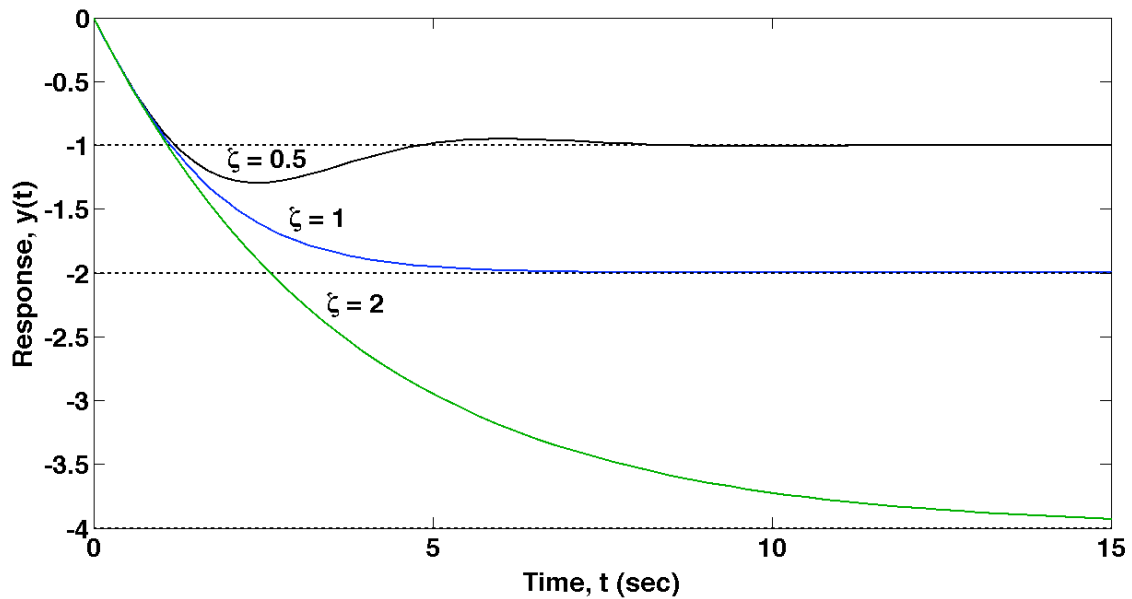
The damping ratio, ζ , of a mechanical mass-spring-damper system is defined as the ratio of the actual damping value to the critical damping value of the system. The damping ratio determines whether the system will experience oscillatory behavior. For instance, an underdamped system having a damping ratio less than 1 will experience oscillatory behavior, whereas a system that is critically damped ($\zeta = 1$) or overdamped ($\zeta > 1$) will not. Therefore, the goal of modeling a fluidic system comprised of colliding drops in terms of spring and damping elements is to create an effective damping ratio, based entirely on known system parameters and initial conditions, that can accurately predict whether the liquid drops will bounce apart from one another or coalesce upon collision. This effective damping ratio was derived in Chapter 3, and this section aims to compare and contrast the results from the

mechanical and fluidic models as a means of testing the validity of the analogy.

Regardless of the orientation of the spring and damping elements in a mechanical system, the damping ratio is defined such that underdamped always corresponds to $\zeta < 1$ and overdamped always corresponds to $\zeta > 1$. It has been shown that the mechanical system considered herein has a damping ratio of $\zeta = \sqrt{(km)/(2b)}$, which is essentially the inverse of the damping ratio for the more common mechanical system comprised of spring and damping elements arranged in a parallel configuration (where $\zeta = b/(2\sqrt{km})$). The responses of these two systems are compared in Figure 27.



(a)



(b)

Figure 27: (a) System response of mechanical mass-spring-damper system with parallel configuration (b) System response of mechanical mass-spring-damper system with series configuration.

The results presented in Figure 27 compare the responses of two mechanical systems with different configurations under the same exact conditions; that is, both systems had an impulsive force (downward) applied to the mass. The results conform that despite the configuration of the mechanical elements, a system that is underdamped ($\zeta < 1$) will indeed show oscillatory behavior. Figure 27(b) shows the response of the Maxwell model with an attached mass, which is the system that is used to model the fluidic systems discussed throughout this study.

The effective damping ratio of the mechanical system that models the fluidic system consisting of a planar body approaching a deformable surface is given by Equation (41) (derived in §3.3), which is shown below:

$$\zeta^* = \frac{\sqrt{km}}{2b^*} = \frac{\sqrt{k_w \mu L^3}}{2\sqrt{24mV_0^{3/2}}} \quad (41)$$

For a mechanical mass-spring-damper system, the transition between oscillatory behavior and non-oscillatory behavior is given by $\zeta = 1$. Similarly, the effective damping ratio of the analogous mechanical system should also correspond to $\zeta^* = 1$ at the transition between "Rest" and "Rebound"/"Coalescence" (recall coalescence is observed only during the rebound phase of the symmetric approach of two non-planar fluidic bodies, hence the combining of the two outcomes). Equation (41) may be rewritten in terms of the Weber number, We , and a modified Reynolds number, Re^* , defined by $Re^* = \rho_1 V_1 L / \mu_g$. This modified Reynolds number represents the relative importance of the fluidic body inertia to the gas viscosity (Bach, Koch, & Gopinath, 2004). Substitution of these two parameters reveals the following form of the effective damping ratio:

$$\zeta^* = \frac{392.12}{\sqrt{We \cdot Re^*}} \quad (42)$$

where the factor of 392.12 is the combination of the numerical coefficients that multiply a number of the parameters given in Equation (41), such as the mass and spring constant. From Equation (42), the condition of $\zeta^* = 1$ corresponds to the condition $We \sim 153,760/Re^*$. This condition, therefore, should serve as the threshold between oscillatory and non-oscillatory behavior, or "Rest" and "Rebound". To test this, collision maps have been created that plot the outcome of a wide range of collisions under various sets of system parameters.

A collision map comprised of results obtained from both fluidic models (i.e. a planar body approaching a non-deformable surface and the symmetric approach of two deformable, cylindrical bodies) is shown in Figure 28.

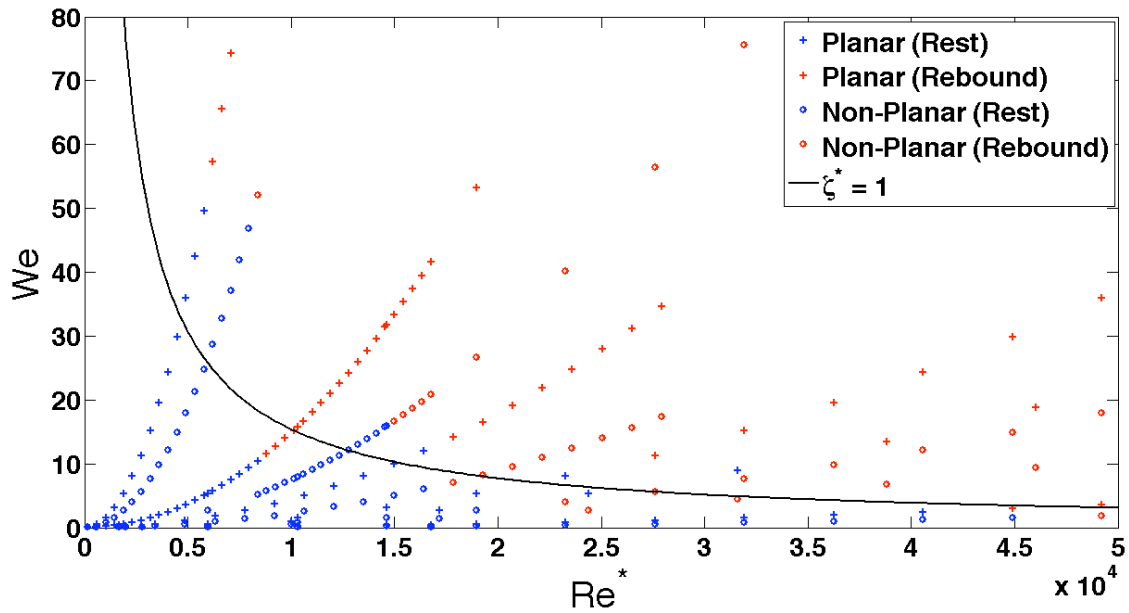


Figure 28: Collision map of fluidic models.

The above collision map shows that indeed the theoretical condition of $We \sim 153,760/Re^*$ very accurately determines the transition between “Rest” and “Rebound” for both fluidic models discussed in this treatment. Naturally, the two models do not coincide exactly with one another, and there are a number of possible reasons for this. First, the factor of 392.12 in Equation (42) would be slightly different for the model of two cylindrical bodies approaching one another since there are two deformable interfaces in that scenario, and hence the effective spring constant should be doubled (this corresponds to an additional factor of $\sqrt{2}$, which is negligible for the

purposes of the present analysis). Second, it has been shown that indeed the shape and evolution of the surface deformations have a significant effect on the collision outcome. Therefore, it is reasonable to expect that a different initial surface shape would also affect the collision outcome. However, the fact that the two fluidic models agree reasonable well with one another suggests that the simpler model of a planar body approaching a deformable surface is a good approximation of the drop-collision process.

Finally, in order to show that the analogy between the fluidic models and a mechanical mass-spring-damper system model is appropriate, a collision map comprised of the results of the analogous mechanical model was also created. This collision map is shown in Figure 29.

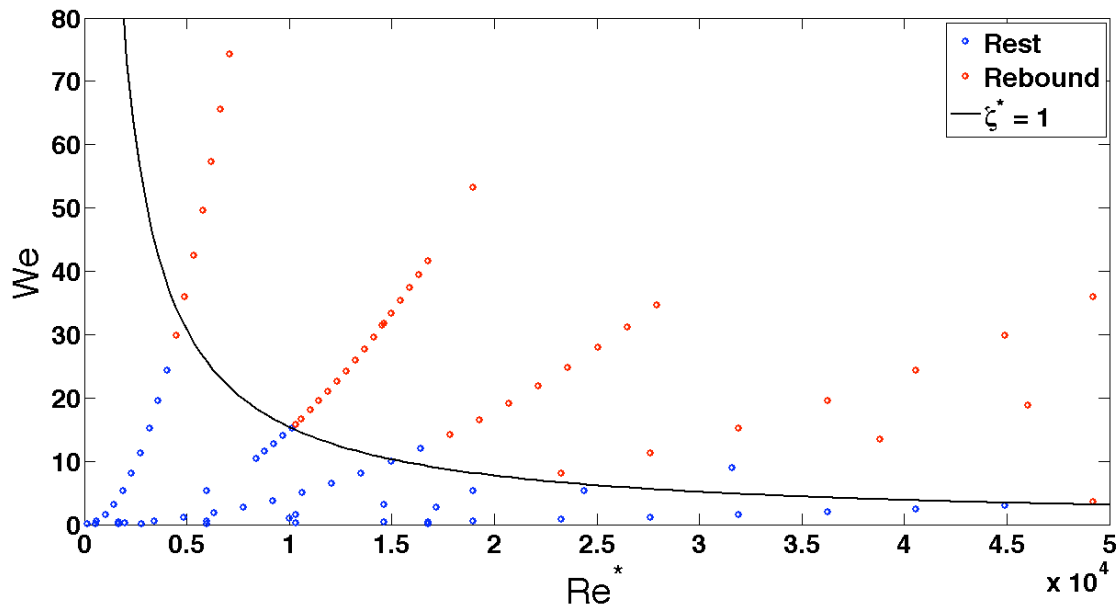


Figure 29: Mechanical mass-spring-damper system collision map.

Figure 29 shows that the mechanical system behaves virtually identically to the fluidic models. Recall that the system parameters (k , b , m , etc.) used to define the mechanical mass-spring-damper system was adopted from the fluidic model of a planar body approaching a deformable surface. Therefore, it may be concluded that a mechanical mass-spring-damper system, whose system parameters are adopted directly from a fluidic model, can accurately predict the outcome of the corresponding fluidic system. The capability of the mechanical mass-spring-damper system to predict the outcome of an actual drop-drop collision depends entirely on the accuracy of the fluidic model upon

which it is based. To this end, the following section compares the predictions of the mechanical system to experimental studies of previous investigators.

5.5 COMPARISON WITH EXPERIMENTAL RESULTS

The theoretical transition between “Rest” and “Rebound” derived in the previous section may be compared to other theoretical and experimental transition conditions reported by previous investigators.

Table 3: Comparison between various experimental results.

Author (Year)	Liquid	Liquid Density [kg/m ³]	Liquid Surface Tension [N/m]	Ambient Gas Viscosity [Ns/m ²]	Drop Diameter [m]	Critical We at Transition (based on D)	Critical Velocity at Transition [m/s]	Re*	We*Re*	% Difference from Prediction
Estrade (1999)	Ethanol	7.89E+02	2.23E-02	1.79E-05	(80--300)E-06	4.57	1--0.5	6.28E+03	2.87E+04	81.34%
Bush (2009)	Water/Soap	1.05E+03	2.36E-02	1.79E-05	1.60E-03	2.00	0.168	1.57E+04	3.15E+04	79.54%
Brazier-Smith (1971)	Water	1.00E+03	7.21E-02	1.79E-05	5.30E-04	4.24	0.759	2.25E+04	9.53E+04	37.99%
Qian and Law (1997)	Hydrocarbon	7.58E+02	2.60E-02	1.79E-05	1.31E-04	0.50	0.362	2.01E+03	1.00E+03	99.35%
Wang (2008)	Water	1.00E+03	7.21E-02	1.79E-05	2.60E-03	2.89	0.283	4.11E+01	1.19E+02	99.93%

Table 3 lists the results of several past experiments that studied the approach and collision of liquid drops. The reported transition between slow coalescence and rebound from each study has been reformulated in terms of the $WeRe^*$ product, which allows for a direct comparison to the theoretical transition condition proposed in this treatment. Some important notes should be made regarding the results listed in Table 3. The study conducted by Estrade, et al. gave only ranges of values for the system parameters used in their experiment, such as drop size and

approach velocity. Therefore, precise combinations of approach velocity and drop size that result in bounce or coalescence are not known. For that reason, average values of drop size and velocity were used to determine the critical value of Re^* (however, the critical We was given as approximately 4.57, as listed). It should also be noted that in some cases, the precise criteria for transition between rebound and slow coalescence was not given. Therefore, the set of conditions under which rebound was first observed was used as this threshold.

As shown in Table 3, the criteria for transition between "Rest" and "Rebound" presented here varies significantly from other studies in terms of percent difference. However, it should be noted that the product of $WeRe^*$ is proportional to the approach velocity cubed. Therefore, a rather large percent difference between $WeRe^*$ values corresponds to a much smaller percent difference in terms of approach velocity. For example, a percent difference in terms of the $WeRe^*$ of 100% corresponds to a percent difference of approximately 25% in terms of approach velocity, which is relatively small.

Chapter 6

Conclusions

For a number of reasons, microfluidics is an increasingly important area of research for many investigators, especially for those involved in the biological sciences. An important problem that has been studied rather extensively and serves as the basis of the present treatment is the problem of understanding the physics involved in the approach and collision of liquid drop pairs and predicting the outcome of the collision. The collision of liquid drops involves the transfer of kinetic energy to surface energy in the form of surface deformation, which may then be transferred back to kinetic energy via the rebound of the colliding bodies.

It has been shown that the complex system of colliding drops may be modeled by a simple squeeze-flow problem involving planar geometry. Because of the nature of the collision process, an analogy between the fluidic system of colliding drops and a mechanical mass-spring-damper system has been proposed. The results of several different fluidic systems were then compared to results of a mechanical system whose parameters were adopted directly from the fluidic systems' governing equations, which provided validity to the analogy. This analogy resulted in

the derivation of an effective damping ratio, dependent only upon known system parameters and initial conditions. The effective damping ratio, ζ^* , may be used to predict the outcome of a pair of liquid drops; that is, the value of the effective damping ratio determines whether a pair of liquid drops will coalesce upon collision or rebound apart from one another. The ability to predict the outcome of a drop-pair collision may be very useful in the study of a wide range of microfluidic applications.

The present analysis may be further expanded to account for three-dimensional effects during the drop-collision process as well as compressibility effects of the intervening gaseous film. However, comparisons with previous experimental results as reported by a number of investigators shows that the model derived in this treatment may be used with little error, despite the number of simplifying approximations that were applied throughout the analysis.

Appendices

APPENDIX A: DERIVATION OF GOVERNING EQUATIONS FOR A DISK-SHAPED AND CYLINDRICAL BODY APPROACHING A NON-DEFORMABLE SURFACE

Disk-Shaped body of radius R approaching non-deformable surface

Following the derivation of a planar body approaching a non-deformable surface (§2.1), a control volume analysis yields the following velocity profile within the intervening film:

$$u = \frac{z}{2\mu} \frac{dP}{dr} (z - h) \quad (A1)$$

where z and r represent the vertical and radial directions in cylindrical coordinates. The volumetric flow rate of the film is then found via integration of Equation (A1), that is

$$Q = \int u dA, dA = 2\pi r dz$$
$$\therefore Q = -\frac{\pi r h^3}{6\mu} \frac{dP}{dr} \quad (A2)$$

The rate of change of the control volume for this particular situation is $\pi r^2 (dh/dt)$. Continuity requires that the rate of change of the control volume must equal the volumetric flow rate given by Equation (A2). This

allows for the calculation of the following pressure gradient within the control volume:

$$\frac{dP}{dr} = -\frac{6\mu r \dot{h}}{h^3} \quad (\text{A3})$$

Integration of Equation (A3) with application of the boundary condition $P(r=R) = P_0$ yields

$$P(r) - P_0 = -\frac{3\mu R^2}{h^3} \dot{h} \left[\left(\frac{r}{R} \right)^2 - 1 \right] \quad (\text{A4})$$

The damping force may then be obtained via integration of Equation (A4) over the area of the approaching body, where the differential area, $dA = 2\pi r dr$. The damping force is found to be

$$F_d = \frac{3\pi\mu R^4}{h^3} \frac{dh}{dt} \quad (\text{A5})$$

Finally, application of Newton's second law yields the following evolution equation for the position, h :

$$\ddot{h} = \frac{3\pi\mu R^4}{2mh^3} \dot{h} \quad (\text{A6})$$

As mentioned in Section 2.1, the nondimensional equation governing the evolution of the mass position is identical for the case of a disk-shaped body approaching a non-

deformable surface as for the case of a planar body approaching a non-deformable surface. The characteristic time scale used to nondimensionalize Equation (A6) is $t_c = 2m/(3\pi\mu R)$.

Cylindrical body of radius R approaching non-deformable surface

The situation of a cylindrical body approaching a non-deformable surface is shown in Figure A1.

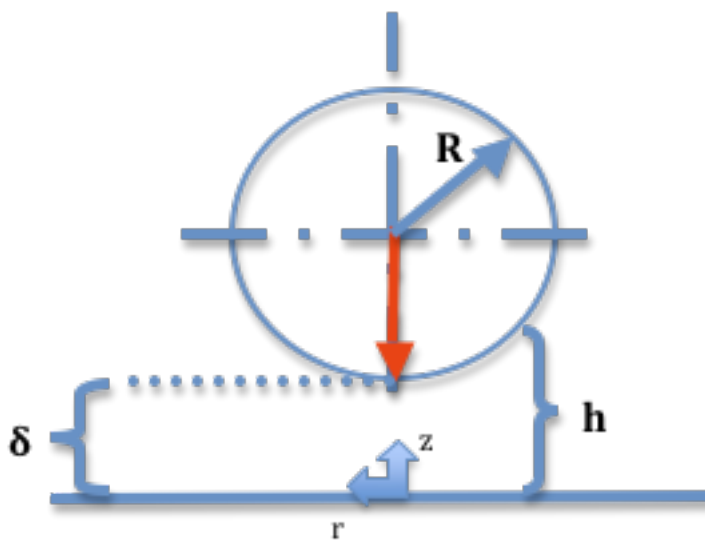


Figure A1: Schematic of cylindrical body approaching non-deformable surface.

As shown, the position of the apex of the cylinder is referred to as δ , whereas the position of the cylinder

surface in general is referred to as h (only at the apex does $h = \delta$). It is approximated that near the apex the shape of the cylinder closely resembles a parabola. Therefore, it is assumed that $h = \delta + r^2/R$.

The present derivation begins with Equation (A3), since the pressure gradient within the film is identical to that from the previous case of a disk-shaped body approaching a non-deformable surface. The pressure distribution is found via integration of Equation (A3), that is

$$P(r) = -6\mu \dot{h} \int \frac{r}{h^3} dr \quad (A7)$$

Substituting for h and performing the integration over r , with the required boundary condition being $P(r=R) = P_0$, yields

$$P(r) - P_0 = \frac{3}{2} \mu R \dot{h} \left[\frac{R^2}{(\delta R + r^2)} + \frac{1}{(\delta + R)^2} \right] \quad (A8)$$

Again, the damping force may be obtained via integration of the pressure distribution over the surface area of the cylindrical body, $A_s = \pi r^2$. Integration yields the following damping force:

$$F_d = 3\pi\mu R \dot{h} \left[\frac{R^2}{2(\delta + R)^2} + \frac{R}{2\delta} - \frac{R^2}{2(\delta R + R^2)} \right] \quad (\text{A9})$$

Recognizing $dh/dt = d\delta/dt$, application of Newton's law results in the following evolution equation for the position of the approaching cylindrical body in terms of the apex position, δ :

$$\ddot{\delta} = \frac{3\pi\mu R}{m} \dot{\delta} \left[\frac{R^2}{2(\delta + R)^2} + \frac{R}{2\delta} - \frac{R^2}{2(\delta R + R^2)} \right] \quad (\text{A10})$$

Equation (A10) may be nondimensionalized by introducing the characteristic time scale, $t_c = m/(3\pi\mu R)$, which results in the nondimensional evolution equation given by Equation (A11).

$$\ddot{\bar{\delta}} = \frac{\dot{\bar{\delta}}}{2} \frac{(2\bar{\delta} + 1)}{\bar{\delta}(\bar{\delta} + 1)^2} \quad (\text{A11})$$

APPENDIX B: TRANSFER FUNCTION ANALYSIS OF MASS-SPRING-DAMPER SYSTEM

The set of equations that govern the motion of the mechanical mass-spring-damper system discussed in Section 3.2 is

$$\begin{aligned}m \ddot{y} &= -b(\dot{y} - \dot{\delta}) + f(t) \\ -k\delta - b(\dot{\delta} - \dot{y}) &= 0\end{aligned}\tag{B1}$$

A Laplace transform analysis may be applied to the above set of governing equations, yielding the following set of algebraic equations in terms of s :

$$\begin{aligned}mYs^2 &= -b(sY - sD) + F \\ -kD - b(sD - sY) &= 0\end{aligned}\tag{B2}$$

where the capitalized letters represent the Laplace transform of the corresponding variable. Eliminating D from the above set of equations gives

$$-k \left[\frac{(mYs^2 - F)}{bs} + Y \right] - b \left[s \left(\frac{mYs^2 - F}{bs} + Y \right) - sY \right] = 0\tag{B3}$$

Finally, Equation (B3) may be simplified to yield the following Laplace transform of the output function, Y:

$$\frac{Y}{F} = \frac{bs + k}{mbs^3 + kms^2 + bks} \quad (\text{B4})$$

APPENDIX C: MATLAB® CODE

Runge-Kutta 4th order method for solving ODEs

```
function [state_new] = rk4(state, time, tau, state_deriv, param)
% Runge Kutta 4th Order Method for solving ODEs
% User inputs the state, time, time step (tau),
% a function that takes the first derivative of the
% state, and a parameter vector and the function outputs a new state
% vector.

% Calculating parameters (k1, k2, k3, k4) needed for rk4 step:

k1 = tau*feval(state_deriv, state, time, param);

temp_xx = state + .5*k1;
k2 = tau*feval(state_deriv, temp_xx, time+tau/2, param);

temp_xx = state + .5*k2;
k3 = tau*feval(state_deriv, temp_xx, time+tau/2, param);

temp_xx = state + k3;
k4 = tau*feval(state_deriv, temp_xx, time+tau, param);

state_new = state + k1/6 + k2/3 + k3/3 + k4/6;
```

Case A: Planar body approaching non-deformable surface

```
global mu LL L mm w

rhs_file = input('Enter file for rhs in single quotes: ');

% Initial conditions for ODE

hh(1) = input('Enter initial height: ');
dhdt(1) = input('Enter initial velocity: ');
state = [hh(1) dhdt(1)];
state_deriv = feval(rhs_file, state, 0, 0);
dh2dt2(1) = state_deriv(2);

% Time-grid setup

dt = 1e-3;
timesteps = 2/dt;

% Space-grid setup

L = 300E-6;
LL = L/2;
dx = LL/50;
```

```

xx = [L/2:-dx:0];
spacesteps = numel(xx);
params = 0;
iplot = 1;
tplot(1) = 0;

% Initial conditions and constants

P0 = 101325;
mu = 1.79E-5;
nu = 1.46E-5;
rho_air = 1.23;
rho_water = 1000;
mm = rho_water*(4/3)*pi*(LL)^3;
w = 1000*L;
for j = 1:spacesteps
P(1,j) = P0;

end

% Nondimensional Scales

l_c = L;
t_c = mm/(mu*w); % For plate situation
t_c = 2*mm/(3*pi*mu*LL); % For disk situation
t_c = mm/(3*pi*mu*LL); % For cylindrical situation

for i = 1:timesteps;

iplot = iplot + 1;

state = rk4(state, (i-1)*dt, dt, rhs_file, params);
state_deriv = feval(rhs_file, state, i*dt, params);
tplot(iplot) = i*dt;
hh(iplot) = state(1);
dhdt(iplot) = state(2);
dh2dt2(iplot) = state_deriv(2);

if hh(iplot) == 0
break
end
end

Possible rhs file's:

% Plate/Disk-shaped body approaching non-deformable surface (Governing
% equations are identical for both cases)

function [state_deriv] = disk_nd(state, time, params)

hh = state(1);
first_deriv = state(2);
second_deriv = -first_deriv/hh^3;

```

```

state_deriv = [first_deriv second_deriv];

% Cylindrical body approaching non-deformable surface

function [state_deriv] = sphere_nd(state, time, params)

hh = state(1);

first_deriv = state(2);
second_deriv = -first_deriv/2*( (2*hh + 1) / (hh*(hh+1)^2) );

state_deriv = [first_deriv second_deriv];

Case B: Planar body approaching deformable surface

% This program uses an iterative scheme to resolve the film
% characteristics between a planar body and a deformable surface.

rhs_file = 'name of file'; % See below for rhs file used for Case B
delta_rhs_file = 'name of file'; % See below for rhs file used for
% calculating the deformation of the surface

% Constants

global mu rho sigma P0 w mm L LL P_c l_c t_c xx dx

mu = 1.79E-5; % viscosity of air [Ns/m^2]
nu = 1.46E-5; % kinematic viscosity of air [m^2/s]
rho = 1000; % density of water [kg/m^3]
sigma = 7.21e-2; % interfacial tension of water [N/m]
P0 = 101325; % [Pa]
L = 300e-6;
w = 1000*L; % width [m]

% Space-grid setup

LL = L/2;
dx = LL/50;
xx = [0:dx/L:LL/L];
spacesteps = numel(xx);
mm = 4/3*pi*LL^3*rho;

% ND Scales

P_c = mu^2*w/(mm);
t_c = mm/(mu*w);
l_c = L;

% Initial conditions

V0 = -1.5; % [m/s]
h0 = 2*L;

```



```

hh(1) = h0/l_c;
dhdt(1) = V0*t_c/l_c;
dh2dt2(1) = 0;
Force(1) = 0;

% Time-grid setup

dt = 1e-3;
timesteps = .2/dt;
tspan = [0:dt:timesteps*dt];

for j=1:spacesteps
delta(1,j) = 0;
PP(1,j) = P0/P_c; % abs P
RR(1,j) = 1000;
ddelta_dx(1,j) = 0;
ddelta_dt(1,j) = 0;
end
We(1) = (rho*(V0)^2*L)/sigma;
Re(1) = abs(rho*V0*L/mu);
Oh = mu/(rho*L*sigma)^0.5;
aspect_ratio(1) = hh(1)*l_c/L;
dyn_cond(1) = Re(1)*aspect_ratio(1);

% Main Program

iplot = 1;
state = [hh(iplot), dhdt(iplot)];

for i = 1:timesteps

params = [spacesteps, zeros(1,spacesteps-1); PP(iplot,:); RR(iplot,:)];

state = rk4(state, (i-1)*dt, dt, rhs_file, params);
state_deriv = feval(rhs_file, state, i*dt, params);

iplot = iplot + 1;
tplot(iplot) = i*dt;

hh(iplot) = state(1);
dhdt(iplot) = state(2);
dh2dt2(iplot) = state_deriv(2);

We(iplot) = (rho*(dhdt(iplot)*l_c/t_c)^2*L)/sigma; % Weber #
Re(iplot) = abs(rho*dhdt(iplot)*l_c/t_c*L/mu); % Re of film based on
% film thickness
aspect_ratio(iplot) = hh(iplot)*l_c/L;
dyn_cond(iplot) = Re(iplot)*aspect_ratio(iplot);

% Pressure

for j=spacesteps:-1:1
if j==spacesteps

```

```

PP(iplot,j) = P0/P_c;
else
PP(iplot,j) = (dx/l_c)*((j-1)*dx/l_c)*(dhdt(iplot) - ddelta_dt(iplot-
1,j))*...
(-1/6*(hh(iplot)^3 - delta(iplot-1,j)^3) -1/2*(hh(iplot)*delta(iplot-
1,j)^2 - delta(iplot-1,j)*hh(iplot)^2))^(-1)...
+ PP(iplot,j+1);
end
Force(iplot) = trapz(xx*l_c,PP(iplot,:))*P_c-P0)*2*w; % Using gage
% pressure, '2' for symmetry, [N]
RR(iplot,j) = sigma/(PP(iplot,j)*P_c - P0)/l_c;
end

% Deformation

for j=1:spacesteps
if j==1
delta(iplot,j) = 0;
ddelta_dx(iplot,j) = 0;
else
deltastate = [delta(iplot,j-1), ddelta_dx(iplot,j-1)];
deltastate = rk4(deltastate, xx(j), dx/l_c, delta_rhs_file,
RR(iplot,j)); % Inputs ND'ed by l_c
delta(iplot,j) = deltastate(1);
ddelta_dx(iplot,j) = deltastate(2);
end
end

for j = 1:spacesteps
delta(iplot,j) = delta(iplot,j) - delta(iplot,spacesteps);
end

for j=1:spacesteps
ddelta_dt(iplot,j) = ((delta(iplot,j)-delta(iplot-1,j))/dt);
end

% Outcome Conditions

outcome = 'Rest'; % Default outcome
if hh(iplot) - max(delta(iplot,:)) <= 4e-8/l_c % Stop if h reaches ~400
% Angstrom (1 angstrom = 0.01 microns)
outcome = ' Coalesce';
fprintf(outcome)
break
elseif isnan(hh(iplot))==1
outcome = ' NaN';
fprintf(outcome)
break
elseif dhdt(iplot) - ddelta_dt(iplot,1) > 0 && dhdt(iplot) > 0
outcome = ' Rebound';
fprintf(outcome)
break
elseif dh2dt2(iplot) == 0 && dhdt(iplot) == 0

```

```

outcome = ' Rest';
fprintf(outcome)
break
end

```

```

end

```

rhs file for Case B

```

function [state_deriv] = file_rhs(state, time, params)

```

```

global mu P0 w mm P_c LL dx xx l_c

```

```

spacesteps = params(1,1);
PP = params(2,:);
RR = params(3,:);

```

```

hh = state(1);
hh_first_deriv = state(2);

```

```

% Trapezoidal Rule for obtaining force

```

```

Force = 2*trapz(xx,PP-(P0/P_c));

```

```

hh_second_deriv = Force; % ND acceleration

```

```

state_deriv = [hh_first_deriv, hh_second_deriv];

```

rhs file used for deformation calculation

```

function [delta_deriv] = delta_rhs_file(deltastate, xx, RR)

```

```

ddelta_dx = deltastate(2);

```

```

d2delta_dx2 = (1 + (ddelta_dx).^2)^(3/2) ./ RR;

```

```

delta_deriv = [ddelta_dx, d2delta_dx2];

```

Case C: Symmetric approach of two deformable cylindrical bodies

```

% This program uses an iterative scheme to resolve the film
% characteristics between a deformable body (initially circular in
% cross-section) and a plane of symmetry.

```

```

rhs_file = 'name of file';
delta_rhs_file = 'name of file';

```

```

% Both above files are identical for both Case B and Case C

```

```

% Constants

```

```

global mu rho sigma P0 w mm L LL P_c l_c t_c xx dx

```

```

mu = 1.79E-5; % viscosity of air [Ns/m^2]

```

```

nu = 1.46E-5; % kinematic viscosity of air [m^2/s]
rho = 1000; % density of water [kg/m^3]
sigma = 7.21E-2; % interfacial tension of water [N/m]
P0 = 101325; % [Pa]
L = 300e-6;
w = 1000*L; % width [m]

% Space-grid setup

LL = L/2; % Radius
dx = LL/500; % Dimensional dx, this Case requires 500 nodes (50 is
% insufficient)
xx = [0:dx/L:LL/L];
spacesteps = numel(xx);
mm = rho*4/3*pi*LL^3;

% Characteristic Scales

P_c = mu^2*w/(mm);
t_c = mm/(w*mu);
l_c = L;

% Initial conditions

V0 = -1.5; % [m/s], Relative velocity
h0 = 2*L;
hh(1) = h0/l_c;
dhdt(1) = V0*t_c/l_c;
dh2dt2(1) = 0;
for j=1:spacesteps
delta(1,j) = (sqrt(LL^2/l_c^2-((j-1)*dx/l_c)^2));
PP(1,j) = P0/P_c; % abs P
RR(1,j) = -LL/l_c;
Pin(1,j) = PP(1,j) - (sigma/(RR(1,j)*l_c*P_c)); % Internal pressure
ddelta_dx(1,j) = -(1/2)*(LL^2/l_c^2-((j-1)*dx/l_c)^2)^(-1/2)*(-2*(j-
1)*dx/l_c);
ddelta_dt(1,j) = 0;
end
We(1) = (rho*(V0/2)^2*LL)/sigma;
Re(1) = abs(rho*V0/2*L/mu);
Oh = mu/(rho*L*sigma)^0.5;
aspect_ratio(1) = hh(1)*l_c/L;
dyn_cond(1) = Re(1)*aspect_ratio(1);

% Time-grid setup

dt = 1e-3;
timesteps = .3/dt;
tspan = [0:dt:timesteps*dt];

% Main Program

iplot = 1;

```

```

state = [hh(iplot), dhdt(iplot)];

for i = 1:timesteps

for j = linspace(1,timesteps,50)
if i == round(j)
fprintf('%g\n', round(i/timesteps*100))
end
end

params = [spacesteps, zeros(1,spacesteps-1); PP(iplot,:); RR(iplot,:)];

state = rk4(state, (i-1)*dt, dt, rhs_file, params);
state_deriv = feval(rhs_file, state, i*dt, params);

iplot = iplot + 1;
tplot(iplot) = i*dt;

hh(iplot) = state(1);
dhdt(iplot) = state(2);
dh2dt2(iplot) = state_deriv(2);

We(iplot) = (rho*(dhdt(iplot)*l_c/t_c)^2*L)/sigma;
Re(iplot) = abs(l_c*L*dhdt(iplot)/(2*nu*t_c));
aspect_ratio(iplot) = hh(iplot)*l_c/L;
dyn_cond(iplot) = Re(iplot)*aspect_ratio(iplot);

% Pressure

for j=spacesteps:-1:1
if j==spacesteps
PP(iplot,j) = P0/P_c;
else
PP(iplot,j) = (dx/l_c)*((j-1)*dx/l_c)*(dhdt(iplot) - ddelta_dt(iplot-1,j))*...
( (delta(iplot-1,j)^3 - hh(iplot)^3)/3 + hh(iplot)^2*delta(iplot-1,j) -
hh(iplot)*delta(iplot-1,j)^2)^(-1)...
+ PP(iplot,j+1);
end
Force(iplot) = trapz(xx*l_c,PP(iplot,:)*P_c-P0)*2*w;
RR(iplot,j) = (sigma/(l_c*P_c))./(PP(iplot,j) - Pin(1,j)); % Assuming
% Pin = const.
end

% Deformation

for j=spacesteps:-1:1
if j==spacesteps
delta(iplot,j) = 0;
ddelta_dx(iplot,j) = 10; % imposing large value compared to system
elseif j==1
delta(iplot,j) = delta(iplot,j+1); % d_delta/dx = 0 at x = 0

```

```

else
deltastate = [delta(iplot,j+1), ddelta_dx(iplot,j+1)];
deltastate = rk4(deltastate, xx(j), dx/l_c, delta_rhs_file,
RR(iplot,j));
delta(iplot,j) = deltastate(1);
ddelta_dx(iplot,j) = deltastate(2);
end
end

for j = 1:spacesteps
delta(iplot,j) = delta(iplot,j) - delta(iplot,spacesteps);
end

for j=1:spacesteps
ddelta_dt(iplot,j) = ((delta(iplot,j)-delta(iplot-1,j))/dt);
end

% Outcome Conditions

outcome = 'Rest'; % Default outcome
if hh(iplot) - max(delta(iplot,:)) <= 4e-8/l_c %Stop if h reaches ~400
% Angstrom (1 angstrom = 0.01 microns)
outcome = ' Coalesce';
fprintf(outcome)
break
elseif isnan(hh(iplot))==1
outcome = ' NaN';
fprintf(outcome)
break
elseif dhdt(iplot) - ddelta_dt(iplot,1) > 0 && dhdt(iplot) > 0
outcome = ' Rebound';
fprintf(outcome)
break
elseif dh2dt2(iplot) == 0 && dhdt(iplot) == 0
outcome = ' Rest';
fprintf(outcome)
break
end

end

```

Mechanical Mass-spring-damper system

```

% This program uses a state-space approach for modeling a mechanical
% mass-spring-damper system

```

```

global w mu

```

```

equations = 'name of file holding governing equations';

```

```

% Constants

```

```

mu = 1.79E-5; % viscosity of air [Ns/m^2]

```

```

rho = 1000; % [kg/m^3]
sigma = 7.21E-2; % [N/m], interfacial tension of water and air
L = 300e-6; % length, [m]
w = 1000*L; % width [m]
P0 = 101325; % [Pa]

m =rho*4/3*pi*(L/2)^3; % [kg]
k = 4000*sigma;

V0 = -1; % [m/s]
h0 = 2*L; % [m]

h0_crit = abs((w*mu*L^3/(24*m*V0))^(1/2));
b_crit = (w*mu*L^3/(24*h0_crit^3));

% Characteristic scales

l_c = L;
t_c = sqrt(m/k);
b_c = sqrt(k*m);

% Nondimensional parameters

We = rho*V0^2*L/sigma;
Re = rho*abs(V0)*L/mu;
Oh = mu/(rho*L*sigma)^0.5;

zeta = sqrt(k*m)/(2*b_crit) % Damping ratio

% Initial Conditions

x1(1) = h0/l_c;
x2(1) = V0*t_c/l_c;
x3(1) = 0;
tt(1) = 0;

y(1) = x1(1);
d(1) = x3(1);
d_dot(1) = 0;

b(1) = abs(w*mu*L^3/24*( (d(1)*y(1)^2/2 - y(1)^3/6 - d(1)^2*y(1)/2 +
d(1)^3/6)*l_c^3 )^(-1) ) / b_c;

F_d(1) = 0;
F_s(1) = 0;

% Time-Grid setup

dt = abs(x1(1)/x2(1)/10000);
if dt < 0.001
dt = dt;
else
dt = 0.001;

```

```

end
dt = ___; % overwrite dt for computational purposes here if necessary
timesteps = 30/dt;

% Main Program

state(1,:) = [x1(1), x2(1), x3(1)];

for j=1:timesteps

iplot = j+1;
tt(iplot) = j*dt;

b(iplot) = abs(w*mu*L^3/24*((d(j)*y(j)^2/2 - y(j)^3/6 - d(j)^2*y(j)/2 +
d(j)^3/6)*l_c^3)^(-1) ) / b_c;

params = [b(iplot),k,m];
state(iplot,:) = rk4(state(iplot-1,:),tt(iplot-1),dt,equations,params);
state_derivs = feval(equations,state(iplot,:),tt(iplot),params);
d_dot(iplot) = state_derivs(3);

x1(iplot) = state(iplot,1);
x2(iplot) = state(iplot,2);
x3(iplot) = state(iplot,3);

y(iplot) = x1(iplot);
d(iplot) = x3(iplot);

% Forces of interest [N]

F_d(iplot) = -b(iplot)*b_c*(x2(iplot) - state_derivs(3))*l_c/t_c;
F_s(iplot) = -k*d(iplot)*l_c;

% Outcome Conditions

outcome = 'Rest'; % Default outcome
if y(iplot) - d(iplot) <= 400e-10/l_c
outcome = 'Coalesce';
fprintf(outcome)
break
elseif x2(iplot) > 0
outcome = 'Rebound';
fprintf(outcome)
break
elseif x2(iplot) - d_dot(iplot) > 0 && x2(iplot) > 0
outcome = 'Rebound';
fprintf(outcome)
break
elseif isnan(b(iplot)) == 1
outcome = 'NaN';
fprintf(outcome)
break
elseif state_derivs(2) == 0 && x2(iplot) == 0

```



```
outcome = 'Rest';  
fprintf(outcome)  
break  
end  
end
```

Function file holding governing equations for mechanical system

```
function [derivs] = x_deriv(state,time,params)  
  
b = params(1);  
k = params(2);  
m = params(3);  
  
x1=state(1);  
x2=state(2);  
x3=state(3);  
  
derivs(1) = x2;  
derivs(3) = -x3/b + x2;  
derivs(2) = -b*(x2 - derivs(3));
```

References

- Ashgriz, N., & Poo, J. (1990). Coalescence and Separation of Binary Collisions of Liquid Drops. *Journal of Fluid Mechanics* , 221, 183-204.
- Atkinson, K., & Han, W. (2004). *Elementary Numerical Analysis* (3rd Edition ed.). Hoboken, NJ: John Wiley & Sons, Inc.
- Bach, G. A., Koch, D. L., & Gopinath, A. (2004). Coalescence and Bouncing of Small Aerosol Droplets. *Journal of Fluid Mechanics* , 518, 157-185.
- Bradley, S., & Stow, C. (1978). Collisions Between Liquid Drops. *Philosophical Transactions for the Royal Society of London* , 287, 635-675.
- Brazier-Smith, P., Jennings, S., & Latham, J. (1972). The Interaction of Falling Water Drops: Coalescence. *Proceedings of the Royal Society of London* , 326, 393-408.
- Bremond, N., Thiam, A. R., & Bibette, J. (2008). Decompressing Emulsion Droplets Favors Coalescence. *Physical Review Letters* , 100.
- Davis, R. H., Schonberg, J. A., & Rallison, J. M. (1989). The Lubrication Force Between Two Viscous Drops. *Physics of Fluids A: Fluid Mechanics* , 77-81.
- de Gennes, P.-G., Brochard-Wyart, F., & Quere, D. (2004). *Capillarity and Wetting Phenomena: Drops, Bubbles, Pearls, Waves*. (A. Reisinger, Trans.) New York, NY: Springer.
- Edwards, C. H., & Penney, D. E. (2002). *Calculus* (6th Edition ed.). Upper Saddle River, NJ: Prentice-Hall Inc.

Estrade, J., Carentz, H., Lavergne, G., & Biscos, Y. (1999). Experimental Investigation of Dynamic Binary Collision of Ethanol Droplets -- A Model for Droplet Coalescence and Bouncing. *International Journal of Heat and Fluid Flow* , 20, 486-491.

Gilat, A. (2005). *Matlab: An Introduction With Applications* (2nd Edition ed.). Hoboken, NJ: John Wiley & Sons, Inc.

Gilet, T., & Bush, J. W. (2009). The Fluid Trampoline: Droplets Bouncing on a Soap Film. *Journal of Fluid Mechanics* , 625, 167-203.

Gunn, R. (1965). Collision Characteristics of Freely Falling Water Drops. *Science* , 150, 695-701.

Haddad, Y. (1995). *Viscoelasticity of Engineering Materials*. London: Chapman & Hall.

Jeelani, S., & Hartland, S. (1998). Effect of Surface Mobility on Collision of Spherical Drops. *Journal of Colloid and Interface Science* , 206, 83-93.

Kiusalaas, J. (2005). *Numerical Methods in Engineering with Matlab*. New York: Cambridge University Press.

Moore, D. F. (1993). *Viscoelastic Machine Elements: Elastomers and Lubricants in Machine Systems*. Oxford: Butterworth-Heinemann Ltd.

Nikolopoulos, N., Nikas, K., & Bergeles, G. (2009). A Numerical Investigation of Central Binary Collision of Droplets. *Computers and Fluids* , 38, 1191-1202.

Ogata, K. (2004). *System Dynamics* (4th Edition ed.). Upper Saddle River, NJ: Pearson Prentice Hall.

- Orme, M. (1997). Experiments on Droplet Collisions, Bounce, Coalescence and Disruption. *Progress in Energy and Combustion Science* , 23, 65-79.
- Panton, R. L. (2005). *Incompressible Flow* (3rd Edition ed.). Hoboken, NJ: John Wiley & Sons, Inc.
- Post, S. L., & Abraham, J. (2002). Modeling the Outcome of Drop-Drop Collisions in Diesel Sprays. *International Journal of Multiphase Flow* , 28, 997-1019.
- Qian, J., & Law, C. (1997). Regimes of Coalescence and Separation in Droplet Collision. *Journal of Fluid Mechanics* , 331, 59-80.
- Quan, S., Lou, J., & Schmidt, D. (2009). Modeling Merging and Breakup in the Moving Mesh Interface Tracking Method for Multiphase Flow Simulations. *Journal of Computational Physics* , 228, 2660-2675.
- Rayleigh, L. (1896). *The Theory of Sound*. London: Macmillan & Co.
- Richard, D., Clanet, C., & Quere, D. (2002). Contact Time of a Bouncing Drop. *Nature* , 417.
- Schotland, R. (1960). Experimental Results Relating to the Coalescence of Water Drops with Water Surfaces. *Discussions of the Faraday Society* , 30, 72-77.
- Spotts, M., Shoup, T., & Hornberger, L. (2004). *Design of Machine Elements*. Upper Saddle River, NJ: Pearson Education, Inc.
- Wang, F.-C., Feng, J.-T., & Zhao, T.-P. (2008). The Head-On Colliding Process of Binary Liquid Droplets at Low Velocity: High-Speed Photography Experiments and Modeling. *Journal of Colloid and Interface Science* , 326, 196-200.

Weibel, D. B., & Whitesides, G. M. (2006). Applications of Microfluidics in Chemical Biology. *Current Opinion in Chemical Biology* , 10, 584-591.

Yiantsios, S. G., & Davis, R. H. (1991). Close Approach and Deformation of Two Viscous Drops due to Gravity and van der Waals Forces. *Journal of Colloid and Interface Science* , 144, 412-433.

Yiantsios, S. G., & Davis, R. H. (1990). On the Bouancy-Driven Motion of a Drop Towards a Rigid Surface or a Deformable Interface. *Journal of Fluid Mechanics* , 217, 547-573.

Yoon, Y., Baldessari, F., Cenicerros, H. D., & Leal, G. (2007). Coalescence of Two Equal-Sized Deformable Drops in an Axisymmetric Flow. *Physics of Fluids* , 19.

Vita

Paul Van Noordt was born in Rayleigh, North Carolina on December 4, 1984. Shortly thereafter, his family moved to Bayonne, New Jersey where he and his sister, Vicki, were raised by their single-parent mother, Arlene. Paul attended kindergarten through high school in the city of Bayonne, where he graduated with honors from Bayonne High School.

His college career began at the New Jersey Institute of Technology, where he originally enrolled as an Architecture major. After one semester, however, Paul realized he had no artistic talents and changed his major to Mechanical Engineering, a field in which he excelled. While working towards his undergraduate degree in M.E., Paul completed an internship with Abbott Laboratories during the summer of 2006. He graduated from NJIT with a Bachelor of Science in Mechanical Engineering and a completed minor in Applied Mathematics in the fall of 2007. Before arriving at The University of Texas at Austin, Paul worked at Valcor Engineering in Springfield, NJ as a Mechanical Engineer.

Permanent address: 7600 Wood Hollow Dr, Austin, TX, 78731